Impacts of land reclamation on sediment transport and sedimentary environment in a macro-tidal estuary

Zhixin Cheng, Isabel Jalón-Rojas, Xiao Hua Wang, Yue Liu

Journal Pre-proof

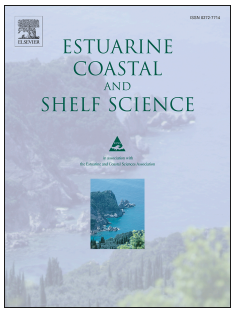

Impacts of land reclamation on sediment transport and sedimentary environment in a macro-tidal estuary

Zhixin Cheng, Isabel Jalon-Rójas, Xiao Hua Wang, Yue Liu

PII: S0272-7714(19)30987-4

DOI: https://doi.org/10.1016/j.ecss.2020.106861

Reference: YECSS 106861

To appear in: *Estuarine, Coastal and Shelf Science*

Received Date: 18 October 2019

Revised Date: 24 April 2020

Accepted Date: 21 May 2020

Please cite this article as: Cheng, Z., Jalon-Rójas, I., Wang, X.H., Liu, Y., Impacts of land reclamation on sediment transport and sedimentary environment in a macro-tidal estuary, *Estuarine, Coastal and Shelf Science* (2020), doi: https://doi.org/10.1016/j.ecss.2020.106861.

Author statement for ECSS_2019_868.

Zhixin Cheng [1,2,*], Isabel Jalon-Rójas [3,1,2], Xiao Hua Wang [1,2] and Yue Liu [4]

[1] The Sino-Australian Research Centre for Coastal Management, The University of New South Wales, Canberra, ACT, Australia

[2] School of Science, The University of New South Wales, Canberra, ACT, Australia

[3] UMR5805 EPOC, CNRS, OASU, Université de Bordeaux, Pessac, France

[4] Urban Construction College, Eastern Liaoning University, Dandong, China

***** Correspondence: Zhixin.Cheng@student.adfa.edu.au; Tel.: +61-45-6308-574

Zhixin Cheng: Conceptualization, Methodology, Software, Visualization, Investigation, Formal analysis, Writing- Original draft preparation.

Isabel Jalon-Rójas.: Methodology, Software, Visualization, Investigation, Writing - Review & Editing.

Xiao Hua Wang: Conceptualization, Resources, Supervision, Writing - Review & Editing.

Yue Liu: Data curation, Resources, Funding acquisition.

Impacts of land reclamation on sediment transport and sedimentary environment in a macro-tidal estuary.

Zhixin Cheng [1,2,*], Isabel Jalon-Rójas [3,1,2], Xiao Hua Wang [1,2] and Yue Liu [4]

[1] The Sino-Australian Research Centre for Coastal Management, The University of New South Wales, Canberra, ACT, Australia

[2] School of Science, The University of New South Wales, Canberra, ACT, Australia

[3] UMR5805 EPOC, CNRS, OASU, Université de Bordeaux, Pessac, France

[4] Urban Construction College, Eastern Liaoning University, Dandong, China

* Correspondence: Zhixin.Cheng@student.adfa.edu.au; Tel.: +61-45-6308-574

Abstract:

During the past decades, extensive coastal areas have been reclaimed along the coastline of China, while the physical mechanisms of human pressures on estuarine-sedimentation are largely unknown. This study investigates the impacts of a land reclamation activity on estuarine sedimentation in the Yalu River Estuary (YE), China. For this purpose, we perform a multidisciplinary approach that combines rare earth element (REE) sediment records and numerical simulations. REE pattern of two sediment core samples from the main estuarine branch changed from diverse to homogenous after the early 1970s, which indicates that the estuarine sedimentary environment experienced dramatic change after the land reclamation activity completed in 1975. In order to explore physical drivers behind this change, hydro-sedimentary dynamics were simulated using Finite Volume Coastal Ocean Model (FVCOM) and an improved Track Marine Plastic Debris (TrackMPD) models. After the land reclamation, model results show that: (1) the degree of flood dominance decreased, and the tidal-choking effect was enhanced in the main branch. (2) The estuary became more well-mixed due to the stronger tidal current; (3) Suspended-sediment concentration (SSC),

especially SSC in the bottom layer was increased. (4) The landward sediment flux caused by tidal pumping decreased significantly and the YE may turn into a sediment source instead of a sink if more land is reclaimed in the future. Furthermore, sediments in the main branch were likely from different sources before reclamation but became a homogenous mixture afterwards. This study qualitatively demonstrates the human-induced impacts on estuarine sedimentation using a multidisciplinary method.

Key words: Yalu River Estuary; FVCOM; sediment transport; particle tracking; numerical simulation; land reclamation.

1. Introduction

Dynamics of suspended sediments affect the morphology, water clarity, light attenuation, and the transport of nutrients and pollutants in an estuary (Byun and Wang, 2005; Dyer, 1997). Thus, quantitative prediction of sediment transport in estuaries is required to provide profound reference for coastal management. In a macro-tidal estuary, the transport of suspended sediments is controlled by tidal dynamics and the erosion of seabed sediments is mainly affected by the bottom tidal current velocity. The natural tidal dynamics in an estuary can be altered by human activities such as mining, dredging, land reclamation and construction of navigation channels and harbours. These human activities modify tidal dynamics through changes of the bottom friction caused by the loss of tidal flats (Gao et al., 2014; Song et al., 2013; Winterwerp et al., 2013), deepening the channel (Dijkstra et al., 2019; Jalón-Rojas et al., 2018; Ralston et al., 2019; van Maren et al., 2015), narrowing the width of waterway (Guo et al., 2017; Moore et al., 2009) and impacts of changing fluvial discharge (Jalón-Rojas et al., 2018).

Such human-induced changes in tides consequently change the local sediment transport, especially in a medium-scale estuary (Byun et al., 2004; Gao et al., 2014; Guo et al., 2017). These changes of sediment transport occur in the sediment resuspension controlled

by tidal current (Li et al., 2014; Winterwerp et al., 2013), the sediment trapping or movement of the estuarine turbidity maximum zone (TMZ) driven by tidal asymmetry (Jalón-Rojas et al., 2015; Song and Wang, 2013) and the sedimentation rate for an estuary to maintain morphological equilibrium (Moore et al., 2009; Williams et al., 2015). For example, in the case of a large-scale human activity such as land reclamation, the suspended-sediment concentration (SSC) was found to be increased greatly in the Ems Estuary (Van Maren et al., 2016); the sediment accumulation rate became larger in the Nakdong Estuary (Williams et al., 2015) and a stronger landward sediment flux was found in the Jiaozhou Bay after reclamation (Gao et al., 2018).

Although recent progress has been made in human impacts on estuarine sediment dynamics, the understanding of this topic in most areas remains vague and unconfirmed due to the lack of historical observations. Elemental analysis from sediment records is an efficient approach to identify the historical events in estuarine sedimentation. Of the various element components in marine sediments, rare-earth elements (REE) contain valid information about sediment provenance due to the stability of their fractionation during weathering and diagenetic processes (Brito et al., 2018; Hathorne et al., 2014; Jung et al., 2012; Orani et al., 2018). REE has been widely-used as a sediment provenance tracer, especially in a dynamic system like the Yellow Sea (Li et al., 2014; Lim et al., 2014; Song et al., 2017; Song and Choi, 2009). And recent studies have also used REE sediment records to investigate historical changes in estuarine environments (Brito et al., 2018; Lim et al., 2014; Martins et al., 2012; Shi et al., 2018; Shynu et al., 2013; Um et al., 2013).

In order to study the physical mechanisms behind the historical changes in estuarine sedimentation, a high-resolution costal ocean model is required. For determining the sediment source-sink relationships in estuaries with limited historical observation, Lagrangian tracking models for sediment particles can be an optimal tool. However, there are

only a few studies using this tool (Lane, 2005; Liubartseva et al., 2018; Souza and Lane, 2013) to track movements of suspended sediment particles, while studies considering the resuspension process of sediments in 3D tracking are even rarer (Lackey and Macdonald, 2007).

This study takes the Yalu River Estuary (YE, border of China, Fig. 1) as an example to study the human impacts on estuarine sedimentation, using REE sediment records together with two numerical models. The YE forms a typical medium-scale, macro-tidal estuarine environment. Previous studies have examined the local characteristics of sediment grain size, ^{210}Pb and ^{137}Cs profiles and heavy-metal in the YE (Chen et al., 2013; Cheng et al., 2019; Gao et al., 2009, 2012, 2003; Liu et al., 2013; Liu, 2016). Characteristics of the REE chemistry in surface sediments in the YE has also been investigated (Liu et al., 2015). However, such analysis must be extended to in-depth sediment samples to explore the historical variation of REE. In terms of the sediment dynamics in the YE, Yu et al. (2014) developed a two-dimensional simplified model to explore the mechanism of turbidity-maxima formation but their results were based on idealized condition; certain details in the three-dimensional (3D) coastal dynamics in this area still remain unknown.

Therefore, this study aims to: (1) reveal historical variation of REE sediment records under anthropogenic influence in the YE; (2) explore the 3D structure of hydrodynamics and sediment transport in this area to discuss the impacts of land reclamation; and (3) track the transport of fine-grained sediments in the YE to investigate the potential changes in sources for bottom sediments.

This study facilitates a more comprehensive understanding of the relevant physical mechanisms of human-induced impacts on estuarine sedimentary environment. Furthermore, an improved 3D particle resuspension and tracking model is proposed in this study, by which we suggest a novel approach to determine the sediment sources in a coastal area.

2. Study area

2.1 Study area

The Yalu River is the largest river flowing into the Northern Yellow Sea (NYS) and contains much terrigenous material. The average annual freshwater and sediment discharge of the river are 2.67×10^{10} m^3 and 1.59×10^{6} T, respectively (Cheng et al., 2016). Materials deposited in the YE and neighbouring area contributes to the bottom sediments in the Yellow Sea (Chen et al., 2013; Shi et al., 2018). The YE can be divided into two branches with three waterways: the West Branch on the west side of Chouduan Island contains the West River and the East Branch consists of the Middle and East rivers with Jiangxin Shoal in the middle (Fig. 1). The underlying tidal ridge system (Fig. 2a) in the YE has an area of 4,000 km^2, extending from the river entrance to the 40m isobaths (Gao et al., 2012), and is associated with parallel tidal ridge areas in the Western Korean Bay (Gao et al., 2016). Governed by that massive tidal ridge, the direction of the flood current in the YE is north-east, that of the ebb current is west-south. Previous study revealed that the sediment source in the YE were a mixture of materials from different regions (fluvial and neritic materials) and the parent rock type of surface sediments in the YE were mainly sedimentary rock and granite (Liu et al., 2015, 2013).

The YE is a macro-tidal estuary, with a mean tidal range of 4.5 m at the entrance (Cheng et al., 2016). The estuary is dominated by regular semi-diurnal tide outside the entrance and irregular semi-diurnal tide with a tidal-river reach of 54 km inside the entrance (Yu et al., 2014). The suspended sediment distribution in the YE is mainly controlled by tides, and there is a TMZ driven by tidal pumping in the lower estuary (Gao et al., 2004; Yu et al., 2014). Due to its strong estuarine hydrodynamics, YE is well-mixed for most of the time except during wet seasons, when there is an extremely large river flow (Cheng et al., 2016; Yu et al., 2014). According to field measurements during 1994, 1996 and 2009, the salinity in

the YRE is well-mixed with no obvious vertical stratification (Cheng et al., 2016; Gao et al., 2004; Yu et al., 2014). Maximum salinity in the upper estuary was around 15 psu during high slacks. Winds and wave action in this area are relatively weak, as the average significant wave height outside the estuary is only 0.5 m (Yu et al., 2014) and the annual mean wind speed is 3.2 m/s (Cheng et al., 2016).

2.2 Reclamation of main islands in the YE

The original Chouduan Island was separated from the Xin Island before 1970, divided in the middle by Yingmen channel (Fig. 2b). The total area of the original Chouduan Island and Xin Island was only 27.5 km^2 according to a joint measurement by the Chinese and North Korean governments in 1956. In order to obtain more farmland, the major water channel between the two islands, Yingmen Channel, was blocked by the North Korea in 1967 (Cheng, 2007). After that, the water flowing irregularly between the islands was gradually diverted into the main water channel (the current Middle River). The lack of water between the islands uncovered the tidal flats below. Thus, the area of exposed flats increased significantly surrounding the Chouduan Island. Starting with this exposing island surface, a massive land reclamation around Chouduan Island was begun by the North Korean government in 1970. After the completion of the land reclamation in 1975, the Chouduan Island was connected to the Xin Island and expanded to a much larger total area of 80 km^2 (Fig. 2c).

3. Methods

3.1 Field measurements

3.1.1 Sediment-samples collection

Two sediment cores (K1 and K12) were collected in August 2014 in the YE (Fig. 1). K1 (124°20’25”E, 39°48,15”N) is located in the shallow sea area of the YE. K12

(124°19’4”E,39°50’20”N) is located in the lower estuary, at the southern edge of the TMZ observed by previous studies (Gao et al., 2004; Yu et al., 2014). The gravity corers were 4m-long PVC tubes with an inner diameter of 85 mm and an outer diameter of 90 mm. The core samples were collected by pushing the corers into the bottom sediments with the help of laboratory technicians. Sampling was carried out during low slack water, when the water depth was less than 1 m. The major lithologic characteristic of the two samples is clayey silt, with a clay content of 20%–40%. The core samples were then divided into sub-samples at 4–6 cm interval for REE detection, radioactive chronology testing and grain size analysis.

Surface sediment samples were collected from four sections around the YE using clamshell-type samplers (Fig. 1). Forty surface sediment samples from the Middle and West waterways and adjacent area (Sections A, B, C and E in Fig.1) were collected from June to August 2006; eleven surface sediment samples were collected from the tidal flats outside the entrance in July 2010 (Section D). These surface samples have been analyzed by Liu et al. (2015), and here we use sectionally averaged REE concentrations of these samples as additional information to our core samples.

3.1.2 Hydrodynamics data collection

A field survey for hydrodynamic observations was conducted in the YE during the wet season (August) of 2009. Water level, turbidity, current velocity and direction were measured at a ship-based anchor station Y03 (124° 16′ 43″ E, 39° 50′ 22″ N) over a continuous 25h period during spring tide (8–9 August) and neap tide (14–15 August). Same properties were also measured at station Y02 (124°18′ 10″ E, 39°55′ 12″ N; Fig. 1) during spring tide (7–8 August) and neap tide (13–14 August). The current and water level were measured by Acoustic Doppler Current Profilers (ADCP) with a frequency of 1200 kHz and a current-speed resolution of 0.001 m/s. The receivers of the ADCPs were placed 0.1 m below the water surface, facing downward, with a bin-layer depth of 0.25 m. Turbidity data

were observed using a multi-parameters water quality probe YSI6600. The measured turbidity was converted into SSC according to in situ filtered water samples collected hourly (Cheng et al., 2016).

3.2 Sediment records of REE

3.2.1 REE concentrations

The divided sub-samples (Section 3.1.1) were first air dried at room temperature (27 °C), then ground using an agate mortar. The ground materials were filtered through a nylon sieve with a diameter of 0.107 mm to eliminate the effect of size differences on the REE measurements. In order to remove the bulk component (e.g. authigenic carbonate, apatite and Fe-Mn oxides) in the sediment samples, the filtered samples were ignited at a temperature of 450ºC, acid pickled using HCl, and then dissolved in a mixed acid of HF and HNO_3. Finally, the dissolved sample solutions were transferred into polyethylene test tubes, and the REE concentrations was then determined using inductively coupled plasma mass spectrometry (ICP-MS). To ensure the accuracy of the testing, repeat samples were tested concurrently with the standard samples. For all 14 elements, the relative errors and the differences between the repeat samples and standard samples were less than 6% and 7.7%, respectively, indicating the satisfactory data reliability.

3.2.2 Grain size analysis and chronology of sediment records

The ^{210}Pb and ^{137}Cs radioactive decay curves of sediment cores K1 and K12 were tested in the State Key Laboratory of Lake Science and Environment, Nanjing Institute of Geography & Limnology, Chinese Academy of Sciences, based on γ-ray spectrum analysis (Cheng et al., 2019). The $^{210}Pb_{ex}$-based sedimentation rates were estimated using the Constant Initial Concentration (CIC) mode (Appleby, 1997; Szmytkiewicz and Zalewska, 2014) and the ^{137}Cs-based sedimentation rates calculated according to the key time markers of ^{137}Cs in the YE (more details can be found in Cheng et al., 2019). For core K1, the $^{210}Pb_{ex}$-based

sedimentation rate was 1.80cm/yr and the ^{137}Cs-based sedimentation rate of K1 1.61 cm/yr. The $^{210}Pb_{ex}$-based and ^{137}Cs-based sedimentation rates for K12 were 1.80 cm/yr and 1.88 cm/yr, respectively. As the sedimentation rates from each core found using the two different methods were similar, this study used the ^{137}Cs-based sedimentation rates to determine the age of every layer in the two cores.

A laser particle size analyzer BT-9300HT was used to measure sediment grain size in the cores. Sediment samples were first put into water and allowed to sit for 24 hours, then 10–20 ml of $(NaPO_3)_6$ dispersant at a concentration of 0.05 mol/L were added. Determination of particle grain size was then conducted using the Collias equal-moment formula (Collias, 1943).

3.2.3 REE elemental analysis

The REE enrichment values in the YE samples were normalized by corresponding values from the North American Shale Composite (NASC); this reveals the fractionation patterns of the REE during sedimentation (Hannigan et al., 2010; Um et al., 2013). Sectional-averaged REE concentrations from surface sediment samples in the YE and that of the reference samples are shown in Table 1.

Some characteristic coefficients of REE, known as fractionation factors, are widely-used to demonstrate the fractionation properties among elements. NASC-based normalized REE concentrations were used to calculate the REE fractionation factors δEu_{NASC}, δCe_{NASC}, $(La/Sm)_{NASC}$, $(Gd/Yb)_{NASC}$ and $(La/Yb)_{NASC}$ in this study.

The Eu and Ce anomalies (δEu and δCe) are given in terms of the relevant concentrations as (Leybourne and Johannesson, 2008):

$$\delta Eu = (Eu_N)/\sqrt{(Sm_N\ Gd_N)}\,, \quad (1)$$

$$\delta Ce = (Ce_N)/\sqrt{(La_N\ Pr_N)}\,, \quad (2)$$

where N denotes the normalization method (using the NASC sample here). The anomaly level

of Ce and Eu can be estimated according to the closeness of the values to 1 (no anomaly).

This study focuses on the lanthanides of REEs from La to Lu and can be divided into two groups: light REE (La, Ce, Pr, Nd, Sm and Eu) and heavy REE (Gd, Tb, Dy, Ho, Er, Tm, Yb and Lu). $(La/Yb)_N$ indicates the fractionation property between the light REE (LREE) and heavy REE (HREE): the larger the ratio, the higher the relative enrichment level of the LREE. $(La/Sm)_N$ indicates the internal fractionation property in the LREEs: the larger the ratio, the more obvious the fractionation is. $(Gd/Yb)_N$ indicates the internal fractionation property in the HREEs: the larger the ratio, the more obvious the fractionation is.

3.3 Numerical simulations

3.3.1 FVCOM model

Hydrodynamic simulation

A 3D hydrodynamic model, the Finite Volume Coastal Ocean Model (FVCOM) (Chen et al., 2003) was used to explore the hydrodynamic changes in the YE after the land reclamation.

FVCOM adopts an unstructured, triangular grid to depict land boundaries with wet/dry treatments (Ge et al., 2012), which provides an accurate simulation of the irregular coastline and massive tidal flats in the YE region. The Mellor and Yamada level 2.5 (MY-2.5) (Mellor and Yamada, 1982) and Smagorinsky turbulent closure schemes (Smagorinsky, 1963) are used in this model for vertical and horizontal mixing, respectively. The governing equations including momentum, continuity, temperature, salinity and density are given in Chen et al (2013).

Sediment simulation

The UNSW-Sed sediment module which considers the effect of sediment stratification in the bottom boundary layer (BBL) has been coupled with the hydrodynamics

model to obtain further accuracy. Following the sediment model developed in Wang (2002), sediment transport in UNSW-Sed for FVCOM in a sigma coordinate system can be described by:

$$\frac{\partial}{\partial t}(CD) + \frac{\partial}{\partial x}(CuD) + \frac{\partial}{\partial y}(CvD) + \frac{\partial}{\partial \sigma}[C(w + w_s)] = \frac{\partial}{\partial x}\left(HA_{\square}\frac{\partial C}{\partial x}\right) + \frac{\partial}{\partial y}\left(HA_{\square}\frac{\partial C}{\partial y}\right) + \frac{\partial}{\partial \sigma}\left(\frac{K_{\square}}{D}\frac{\partial C}{\partial \sigma}\right), \quad (3)$$

where t and D represent time and water depth, C is the SSC and w_s is the particle settling velocity, which is not affected by the transformation from a Cartesian coordinate system to the sigma-coordinate system. $A_{\square}$ and $K_{\square}$ are horizontal and vertical turbulent eddy viscosities, respectively.

With the contribution of the re-suspended sediments in nepheloid layer, the density of sea water can be expressed as:

$$\rho = \rho_w + (1 - \frac{\rho_w}{\rho_s})C, \quad (4)$$

where ρ_w is the density of clear seawater, and ρ_s the sediment density.

The flux Richardson number was introduced into the bottom friction coefficient C_d to consider the effects of the sediment-induced BBL in the model (Wang, 2002):

$$C_d = [\frac{1}{\kappa/(1+AR_f)}\ln\frac{(H+z_b)}{z_0}]^{-2}, \quad (5)$$

where κ = 0.4 is the von Kármán constant; and R_f is the flux Richardson number, indicating the vertical density stratification in the Mellor-Yamada Level 2 approximation. A is an empirical constant ranging from 6.8 to 14.7, independent of flow state and R_f; A was set to different values in previous studies (Glenn and Grant, 1987; Soulsby and Dyer, 1981; Wang, 2002). z_o and z_b are the bottom roughness and the thickness of the near-bottom layer.

According to Ariathurai and Krone (1977), the vertical sediment flux at the bottom caused by erosion/deposition processes, E_b, can be expressed as:

$$E_b = \begin{cases} E_0\left(\frac{|\tau_b|}{\tau_c} - 1\right), & \text{if } |\tau_b| > \tau_c \\ C_b w_s(\frac{|\tau_b|}{\tau_c} - 1), & \text{if } |\tau_b| < \tau_c \end{cases} \quad (6)$$

where E_0 is the erosion coefficient (E_0 and w_s are positive here), τ_b the bottom shear stress, τ_c the critical stress for resuspension and deposition, and C_b is the suspended-sediment concentration in the bottom layer. Erosion happens when E_b is positive.

3.3.2 Three-dimensional particle resuspension and tracking model

Track Marine Plastic Debris (TrackMPD)

A 3D Lagrangian particle-tracking model, TrackMPD, was adopted in this study to investigate the potential sediment source in the YE. TrackMPD is a newly developed transport model which simulates the behavior of marine plastic debris, but it can be also used for the transport of suspended sediments. TrackMPD considers processes such as advection, dispersion, windage, sinking, settling, beaching and re-floating of independent particles (Jalón-Rojas et al., 2019). The horizontal position (X) of a particle at time $t + \Delta t$ in TrackMPD can be expressed as:

$$X(t + \Delta t) = X(t) + U\Delta t + R\sqrt{2K_h\Delta t}, \quad (7)$$

where $U = (u, v)$ and K_h are horizontal current vector and diffusion coefficient, respectively. i and j denote unit vectors in the zonal (x) and meridional (y) directions, respectively. R is a random number (from -1 to 1) generated at each time step with an average and standard deviation from 0 to 1, generated at each time step. $X(t)$ is the original horizontal location of the particle at time t. $U\Delta t$ is the advective displacement and $R\sqrt{2K_h\Delta t}$ is the random displacement due to horizontal turbulent diffusion.

The vertical position (Z) at time $t + \Delta t$ is computed as follows:

$$Z(t+\Delta t) = Z(t) + w(t)\Delta t, \quad (8)$$

$$w(t) = w(t) - w_s(t) + \frac{R\sqrt{2K_z\Delta t}}{\Delta t}, \quad (9)$$

where w, w_s and K_z are the vertical velocity, settling velocity and vertical diffusion coefficient, respectively. $Z(t)$ is the original vertical location of the particle at time *t*. Two diffusion coefficients (K_h and K_z) were used in this model: the final term on the right-hand side in Eqs. (7), (9) is from stochastic motion during turbulent diffusion.

TrackMPD can be easily adapted to different ocean models. Jalón-Rojas et al. (2019) used hydrodynamic results in curvilinear grid from the Princeton Ocean Model (POM) as inputs for TrackMPD. Here, we adopted FVCOM results for TrackMPD for the first time by interpolating the unstructured-grid data into rectangular grids. Moreover, instead of using a constant vertical turbulent eddy viscosity (K_z), a time-dependent K_z calculated by FVCOM at every node which was then incorporated into TrackMPD for further accuracy.

Resuspension of deposited particles

It has always been challenging to reproduce the resuspension of particles in a Lagrangian particle-tracking model. In this study, a resuspension module is added to TrackMPD. A tracking particle is resuspended from the seabed when the bottom shear stress at its sink location is larger than the critical erosion stress. Bedload transport for a particle is not considered in this model. The movement of this particle on resuspension is controlled by both sediment settling under gravity and vertical turbulence in the BBL (Ji, 2006). Accordingly, when a deposited particle meets the criteria for resuspension (Eq. 10), the logical of resuspension variable is true (equals 1) and it is placed at the bottom sigma level; its vertical location after resuspension is determined by w_s and K_z as in Eqs. (8) and (9). Correspondingly, the particle will deposit and stay at the bottom when the relating bottom shear stress is smaller than the critical value.

$$Resuspension = \begin{cases} 1, & \text{if } |\tau_b| > \tau_c \\ 0, & \text{if } |\tau_b| < \tau_c \end{cases} \quad (10)$$

3.3.3 Model configuration and validation

Hydrodynamic-sediment model

The simulation domain (Fig. 3) in this study covered the entire YE area, together with part of the NYS. Two experiments with different coastlines, in 1956 (Fig. 3a) and 2011 (Fig. 3b), were designed to simulate the hydrodynamic and sediment-transport conditions before and after the land reclamation, respectively. Simulation meshes were built using the Surface-water Modeling System (SMS), based on coastline and bathymetry data extracted from sea charts from the Navigation Guarantee Department of the Chinese Navy Headquarters in 2011 and coastline in 1956 (Fig. 2b). Maximum and minimum grid sizes of the meshes were 3000 m at the open boundary and 150 m near shore. A uniformed sigma-stretched coordinate system with 20 vertical layers was applied in this model to study the barotropic hydrodynamics in the YE.

Previous studies in similar systems have concluded that the changes in the water depth after land reclamation had a limited effect on the hydrodynamics compared to the changes in coastline (Gao et al., 2014; Guo et al., 2017). In order to eliminate errors generated in the numerical calculations and to isolate the impacts of the land reclamation, the same bathymetry and initial boundary conditions in 2011 were used for Experiments 1 and 2 (pre-reclamation and post-reclamation). Experiment 3 was designed for model validation using the same mesh as in Experiment 2 but with the boundary conditions in 2009 according to period of the field trip (Section 3.1.2).

As mentioned in Section 2.1, the hydrodynamics in the YE region are dominated by tides; therefore, tidal elevation is adopted as the open boundary condition to drive the model.

The tidal elevations at the open boundary were calculated based on selected tidal components including four diurnal (K_1, Q_1, P_1, Q_1), four semidiurnal (M_2, S_2, N_2, K_2), three shallow-water (M_4, MS_4, MN_4) and two long-period components (Mf, Mm). The Harmonic constants for all tidal components were retrieved from the global tidal model TPXO 7.2.

Given that river discharge also impacts the estuarine dynamics, a constant river discharge of 700 m^3/s with a suspended-sediment flux of 0.1 $kg/m^3/s$ from the river (typical value for the Yalu River during the wet season) at 1h interval was used as another boundary forcing in this model. According to field observations, the YE is well-mixed for most of the time as a consequence of the limited water depth and strong tidal action (Cheng et al., 2016; Yu et al., 2014). Therefore, only the barotropic effects of the freshwater input are considered in this model. The initial conditions for sea temperature and salinity in this model used the typical values in the YE during wet season of 25□ and 33 psu, respectively. The influence of wind and wave action in this area is weak and transient, as discussed in Section 2.1.1; therefore, wind and wave forcing were not considered in the model.

The sediment module set for all experiments considers only cohesive sediments, as most suspended sediments are cohesive and are easily transported in an estuary (Brenon and Hir, 1999). Due to the lack of observations for sediment parameters in the YE, the erosion rate and critical shear stress were assumed to be constant over the estuary, with different values tested to best fit the general pattern of the observation data. The mean grain size of sediments in the YE is about 0.06 mm (Cheng et al., 2019) and the mean SSC in the estuary is beneath the threshold for flocculation (Yu et al., 2014). Thus, the settling velocity was estimated to be constant at 1.25×10^{-4} m/s according to Chakraborti and Kaur (2014) and Van Rijn and Kroon (1993). Other values of key model parameters are shown in Table 2.

Experiments 1 and 2 ran for 92 days from 01 May 2011 to 31 July 2011, Experiment 3

for 62 days from 1 July 2009 to 31 August 2009. All experiments have run for 15 days to warm up.

Particle resuspension and tracking model

Two scenarios (pre- and post-reclamation) were designed for TrackMPD in the YE to reproduce the transport of suspended sediment particles before and after the land reclamation. Using forward tracking to determine their subsequent movement, particles were released every hour from five potential source areas (dark-blue points in Fig. 2a). RN, LR, WK, WR and SW (Fig. 2a) indicate five potential sediment source which represent fluvial sediments from the river load (RN), local resuspended sediments from the East Branch (LR), sediments transported from the Western Korean Bay (WK), sediments transported from the West Branch (WR) and sediments from the shallow waters in the Northern Yellow Sea (SW). These five source areas were located around the estuarine main branch and covered particles from almost all directions.

Particles were released from the near-bottom layer over an area of 0.048 km^2 for each release area. A total number of 7,560 particles was released under different tidal conditions (seven days from UTC 0000 22 May 2011 to UTC 0000 28 May 2011), and all particles were tracked for 14 days after release.

The hydrodynamic inputs (*u*, *v*, *w*, water elevation, bottom shear stress and vertical eddy viscosity) for the two scenarios were from FVCOM simulations (Experiments 1 and 2 in previous section). Settling velocity and critical shear stress for resuspension were set to be the same as for the FVCOM sediment model (Table 2). A particle touches the lateral boundary will beach at its final location; a particle sinks at the bottom will be resuspended into the water column when the bottom stress at its sinking location meets Equation (10).

Model validation

Figure 4 shows the comparison between the water-level observations at 1h intervals from the Yalu Park Hydrology Station and that from the model at the north boundary point of the study domain during June 2011. The hydrology station is located upstream in the river (64 km from the estuary entrance, Fig. 1), 15 km north of the model northern boundary. According to the comparison in Fig. 4, modelled surface elevation agreed reasonably well with the measurements. The slight difference between the two timeseries for the surface elevation around 500 h is acceptable, considering the effects of river flow and the spatial separation between the two sites. Table 3 shows comparison of amplitudes and phases between modelled and observed surface elevation for main tidal constituents. According to these harmonic constants of tidal analysis in Table 3, M_2 appeared to be the predominant tidal constituent in the YE, indicating the estuary is dominant by semidiurnal tides. The average discrepancy in amplitude and phase were 0.05m and 11.4°, demonstrating solid agreement between modelled and observed water level.

The model results of Experiment 3 were further validated against the measurements from the field trip in August 2009. Figure 5(a) shows good agreement between the modelled and measured water elevations during spring and neap tides at Stations Y02 and Y03 (Fig. 1). Figures 5(b, c) show good agreement in the streamwise current speed and current direction, with mean correlation coefficients between model results and measurements of 0.87 and 0.85 (Table 4), respectively. Validation of SSC is shown in Fig. 5(d), indicating the model has captured the magnitude and fluctuations over time of the observed SSC. The differences between the measured and modelled SSC at Y02 may be related to freshwater input. While we used the monthly-averaged river flow as model input due to the lack the high-frequency measurements, the real river flow can vary largely during the wet season. The lower SSC observed at Y02 can be the result of the dilution by the instantaneous freshwater discharge as

the field trip was conducted in August. Simulation of the SSC has always been challenging due to the uncertainty in setting the local parameters (e.g. settling velocity and critical bottom stress; Song and Wang, 2013; Xing et al., 2012). The simulated SSC in this study is already more accurate than in the previous study in the YE (Yu et al., 2014). Although the model did not capture the precise values of SSC, it reproduced its first-order variation and is therefore suitable for studying the changes in sediment transport after land reclamation.

3.3.4 Data post-processing

Decomposition method for the suspended-sediment flux

In order to quantitively understand the change in sediment transport after the land reclamation, the suspended sediment flux was decomposed using the mass-transport flux formulation of Dyer (1997). By neglecting high-frequency turbulence, the tidally and sigma-averaged suspended-sediment flux can be quantified as:

$$\langle T\rangle = \frac{1}{T}\int_0^T\int_0^1 hUC\ d\sigma dt = h_0\bar{U}_0\bar{C}_0 + \bar{C}_0\langle h_t\bar{U}_t\rangle + \bar{U}_0\langle h_t\bar{C}_t\rangle + h_0\langle\bar{U}_t\bar{C}_t\rangle +$$

$$\langle h_t\bar{U}_t\bar{C}_t\rangle + h_0\langle\bar{U}_d\bar{C}_d\rangle + \langle\bar{h}_t\bar{U}_d\bar{C}_d\rangle = T1 + T2 + T3 + T4 + T5 + T6 + T7 \quad , \tag{11}$$

where U and C are the velocity (m/s) and SSC (mg/L), respectively, both functions of depth and tidal phase; h is the water depth (m), a function of time, and T is the tidal period (h). Subscript 0 denotes tidally averaged value; t denotes deviation from tidally averaged value; d deviation from the corresponding depth-averaged value; overbar denotes depth-averaged and angle brackets tidally averaged.

The decomposition terms T_1 to T_7 represent the different contributions of the various physical processes affecting sediment transport (Dyer, 1997): T_1 is the flux induced by the residual flow of water (Eulerian residual velocity); T_2 the Stokes drift caused by the tides; T_3 to T_5 are tidal pumping terms produced by tidal phase differences, with T_3 the correlation

term between the tidal level and SSC, T_4 mainly a consequence of lags between sediment erosion and maximum tidal current and T_5 gives the third-order correlation between tidal levels, velocities, and SSC, which characterizes tidal trapping. T_6 and T_7 arise from vertical circulation effects.

Tidal asymmetry

The skewness γ_{M_2/M_4} was used in this study to investigate the change in tidal asymmetry after land reclamation. γ_{M_2/M_4} is calculated using the harmonic-analysis results of the modelled sea surface elevation for 1 lunar month, according to Song et al. (2011):

$$\gamma_{M_2/M_4} = \frac{\frac{3}{2}a_{M_2}^2\, a_{M_4}\cdot sin(2\varphi_{M_2}-\varphi_{M_4})}{\left[\frac{1}{2}(a_{M_2}^2+ a_{M_4}^2)\right]^{\frac{3}{2}}} \quad , \tag{12}$$

where a_{M_2} and a_{M_4} are the amplitudes of the M_2 and M_4 tidal constituents, respectively; φ_{M_2} and φ_{M_4} are the corresponding phases.

4. Results

4.1 Historical variations of REE sediment records in the YE

4.1.1 Profiles of REE fractionation factors

REE fractionation factors including ΣREE, ΣLREE/ΣHREE, $(La/Sm)_{NASC,}$ $(Gd/Yb)_{NASC,}$ $(La/Yb)_{NASC,}$ δCe_{NASC} and δEu_{NASC} (Sections 3.2.3 and 3.2.4) were calculated in this study as indicators of historical changes in sedimentation in the YE. Figure 6 shows the vertical profiles of REE fractionation factors for cores K1 and K12, together with the corresponding ages derived from chronology results (Cheng et al., 2019). For most profiles, there was an obvious turning point at the layer corresponding to the year 1975.

For K1, ΣREE (Fig. 6a) ranged from 180 μg/g to 286 μg/g, with a mean value of 227

μg/g. ΣLREE/ΣHREE (Fig. 6b) ranged from 12.0 to 15.4, with a mean value of 12.5. ΣREE was significantly larger than the average before 1975, then decreased to and remained at the average in the years after. A similar trend was found in the ratio ΣLREE/ΣHREE, with higher values before 1975 and lower values after. For K12, ΣREE ranged from 147 μg/g to 238 μg/g, with a mean value of 202 μg/g (slightly lower than that of K1). ΣLREE/ΣHREE ranged from 10.4 to 13.5, with a mean value of 12.0. In contrast to K1, ΣREE in K12 was smaller than the average before 1975, then increased to the average, close to that of K1, after 1975. ΣLREE/ΣHREE in K12 showed an increasing trend before 1975 and came close to the K1 value after 1975.

δCe_{NASC} of K1 (Fig. 6f) ranged from 0.78 to 0.86, with a mean value of 0.82 (relatively close to 1). There was also an obvious inflection around 1975, with δCe_{NASC} larger than the average before the inflection and smaller after. δEu_{NASC} of K1 (Fig. 6g) was between 0.48 and 0.82, with a mean value of 0.63. The inflection around 1975 layer was also evident in δEu_{NASC} of K1 but with an opposite trend (values were larger after 1975).

δCe_{NASC} of K12 ranged from 0.76 to 0.83 with a mean value of 0.80. The 1975 inflexion was also distinctive in δCe_{NASC} of K12. In contrast to that of K1, δCe_{NASC} of K12 was smaller than average value before 1975, and became larger after. δEu_{NASC} of K12 ranged from 0.52 to 0.95, with a mean value of 0.69. The 1975 inflection was again evident in δEu_{NASC} of K12, with large values before 1975 and small values after.

For the internal fractionation pattern of HREE: $(Gd/Yb)_{NASC}$ (Fig. 6c) of K1 and K12 ranged from 1.19 to 1.56, and 1.05 to 1.40 with mean values of 1.37 and 1.28, respectively. $(Gd/Yb)_{NASC}$ of K1 was generally larger before 1975 than after, while $(Gd/Yb)_{NASC}$ of K12 decreased slightly after 1975.

$(La/Sm)_{NASC}$ (Fig. 6d) demonstrates the internal fractionation pattern of LREE: $(La/Sm)_{NASC}$ of K1 ranged from 1.35 to 1.47, with a mean value of 1.41. $(La/Sm)_{NASC}$ of K12

was between 1.26 and 1.41, with a mean value of 1.33. Pre- and post-1975 change in $(La/Sm)_{NASC}$ was not marked as in the other profiles. For $(La/Yb)_{NASC}$ (Fig. 6e), which reveals fractionation-pattern differences between LREE and HREE: $(La/Yb)_{NASC}$ of K1 was from 1.9 to 2.7, with a mean value of 2.3 before 1975, falling below the average after 1975. $(La/Yb)_{NASC}$ of K12 was between 1.52 and 2.24, with a mean value of 1.98.

For most fractionation factors, the differences between K1 and K12 were large before 1975 but became smaller after that. Accordingly, the sediment cores in this study were divided into two sections (upper and lower) using the 1975 sedimentation layer as the split line.

4.1.2 Normalized REE fractionation curves

The averaged correlation coefficient between mean grain size and ΣREE, ΣLREE/ΣHREE, $(La/Yb)_{NACS}$, $(La/Sm)_{NASC}$ and $(Gd/Yb)_{NASC}$ over all layers from K1 and K12 was 0.1512, indicating that the granularity effect was not significant in these results.

In order to eliminate the potential effects of other factors on REE fractionation, we also compared the geometric shapes of the normalized REE patterns instead of the abundance of the REE. The REE concentrations of representative sedimentation layers from cores K1 and K12, together with those of surficial sediments of five sections (Fig.1), were normalized by values from the NASC (Table 1).

The NASC-normalized REE curves (Figs. 7a, b) of K1 and K12 had a stronger enrichment in LREE comparing to other surface samples. Samples after 1975 in K12 showed a clear larger deficit in Eu than before 1975. Conversely, samples after 1975 in K1 have a smaller Eu deficit than before 1975. Section E showed a distinct curve with significant depletion in Dy, implying REE upstream area may originated from a different source compared to other samples around the estuary. Previous study also showed that the sediments originated from basaltic lava platform in the Yalu River headstream were restrained in the

upper reach of the river after the reservoir construction (Liu et al., 2015), which may explain the distinct fractionation pattern of Section E.

The fractionation patterns of the YE samples were still belong to a same group, indicating a predominant common parent rock type for this area. However, obvious differences can be found before and after 1975 in K1 and K12. As the sediment source in the YE were a mixture of materials from terrigenous sources (fluvial inputs) and neritic sources carried by ocean currents (Liu et al., 2013), the significant changes in the REE patterns may reflect the changes in the composition of this mixture (e.g., the proportion of fluvial and neritic inputs).

4.1.3 Spatial distribution of REE sedimentation

The chart of ΣREE versus ΣLREE/HREE was used here to identify the differences in REE sedimentation between K1 and K12 and to compare the sediment property at these two sites with surface sediments from surrounding areas.

The patch of sedimentation units (scatter points in Fig. 8) at K1 before 1975 was distinct from other samples around the estuary. These sedimentation units were characterized by prominently higher ΣREE and ΣLREE/HREE, suggesting a unique sediment supply contributed to sediments at K1 before 1975. This particular sediment source before 1975 no longer affected K1 afterwards. After 1975, the patch of sediment units in K1 moved to an area with a center point corresponding to a total REE of 220 μg/g and a ΣLREE/HREE around 13. Compared to the surface samples from five sections around the YE, deposits in K1 after 1975 were more similar to the samples from the LP muddy coast (Section C).

According to Fig. 8(b), the patch of sedimentation units at K12 also moved to a similar area as those of K1 after 1975. The change of REE at K12 was not as prominent as K1, but a distinct change can still be identified: sediment in K12 before 1975 had a more complex feature, whereas units after 1975 were more concentrated. In summary, although the

sediments of K1 and K12 were different before 1975, they became similar after 1975.

It is noteworthy that the slight similarity in the REE property after 1975 between the two cores and Section C does not necessarily indicate sediments of K1 and K12 were from Section C after 1975. It only implied that the post-1975 deposits at K1, K12 and Section C may have a common sediment input.

To further analyze the homogeneity of the deposits at K1 and K12, the Discrimination Function (DF) index was calculated in this study. DF has been widely used in REE studies to evaluate the difference between two samples (Jung et al., 2012; Yang et al., 2019). The DF index is given by:

$$DF = |C_1/C_2 - 1|, \quad (13)$$

where C_1 is an REE parameter from one sample and C_2 the same REE factor from a different sample.

In general, the closer the DF index is to zero, the more similar the sedimentary features of the two samples are. REE fractionation factor $\Sigma LREE/\Sigma HREE$ was used to calculate the DF between K1 and K12 for corresponding layers (Fig. 9). The DF curve clearly shows that the deposits in K1 and K12 became more homogeneous after 1975, with a larger DF index, near 0.3, before 1975 and values smaller than 0.1 after 1975.

In conclusion, multiple indicators demonstrated there was a dramatic change in the sedimentation process around 1975 in K1 and K12. These REE sediment records indicated that the properties of sediments in these two cores became homogeneous after 1975. This homogeneity may be an indicator for concurrent sedimentary succession in the YE.

Unlike natural evolution, human activities can rapidly change the estuarine morphology. Previous studies have shown that a change in coastline can alter the hydrodynamics and sediment transport (Byun and Wang, 2005; Gao et al., 2014; Guo et al., 2017; Li et al., 2014). And the dramatic change in 1975 in REE properties in the YE here is

hypothesized as a consequence of the contemporaneous human-induced changes. In particular, it can be related to the substantial increase of the area of Chouduan Island during the 1970s due to the land reclamation and blocking of the lateral water arms.

These activities generated a narrower estuarine entrance which almost certainly changed the hydrodynamics around the East Branch and thus the changes in the sedimentation process. To verify this hypothesis, numerical models for this area were established in this study to simulate the hydrodynamics condition before and after that reclamation.

4.2 Variations of hydrodynamic-sedimentary dynamics in the YE

4.2.1 Changes in hydrodynamics post-reclamation

Figure 10 presents the model depth-averaged current field for Experiments 1 (pre-reclamation) and 2 (post-reclamation) for flood and ebb during spring and neap tides. The tidal current in the YE generally flowed in the northeast-southwest direction, both pre and post land reclamation. After land reclamation, the magnitude of the tidal current in the East Branch area during spring tide increased by 0.08 m/s for both flood and ebb (Figs. 10a-d). It decreased by 0.4 m/s in a small an area to the south of Chouduan Island (Fig. 1) at flood time due to the effects of the prominent headland (Figs. 10a, b). Although not as evident as for the spring tide, the current speed during neap tide also increased slightly by 0.03 m/s after land reclamation (Figs. 10e-h).

In all simulations, the maximum flood current was larger than the maximum ebb current, showing a significant tidal asymmetry in this area with strong flood dominance. The skewness γ_{M_2/M_4} (Section 3.3.4) in the estuarine area was positive in both experiments, indicating the YE was a flood-dominance system both pre- and post-reclamation (Figs. 11a,

586 b). However, γ_{M_2/M_4}around the East Branch decreased from 0.5 to 0.47 in Experiment 2
587 (Fig. 11c), suggesting that the strength of flood dominance in this area was weakened post-
588 reclamation.

589 **4.2.2 Changes in suspended sediment distribution post-reclamation**

590 Figure 12 shows the modelled depth-averaged SSC before and after land reclamation
591 at different tidal phases (flood time, high water, ebb time and low water) during spring and
592 neap tides. The SSC during spring tide was higher than during neap, with maximum values at
593 flood and ebb, and minimum values at slack water, in accordance with previous studies
594 (Cheng et al., 2016; Yu et al., 2014). A TMZ occurred in the seaward part of the East Branch,
595 coinciding with its location in previous observations (Gao et al., 2004; Yu et al., 2014).
596 Controlled by the tidal excursion, this TMZ moved landward during flood phase and seaward
597 during ebb. The position of the TMZ did not change significantly after land reclamation, but
598 its area and strengthen slightly increased. The magnitude of SSC in the East Branch increased
599 by 140 mg/L after land reclamation, as expected from the enhanced bottom shear stress due
600 to the stronger tidal currents.

601 Figure 13 shows the model horizontal distributions of tidally averaged SSC in the
602 surface and bottom layers and their changes pre- and post-reclamation. The horizontal SSC
603 distributions were similar in the YE for the two experiments. However, the SSC in the surface
604 layer in the East Branch was about one third that in the bottom layer, and the difference
605 became more significant after land reclamation. The horizontal gradient of SSC between the
606 inner and outer estuary also became larger post-reclamation.

607 # 5 Discussion

608 In Section 4, we found that REE pattern at K1 and K12 has changed from diverse to
609 homogenous after 1975. Hydrodynamics and the distribution of SSC in the YE also changed
610 greatly because of the concurrent land reclamation. Thus, this section aims to: (1) provide a

physical explanation to that dramatic change in estuarine sedimentation; and (2) determine the sediment source (terrigenous or neritic inputs) of the estuary before and after the land reclamation.

5.1 Effects of tidal-choking on mixing process

Tidal-choking is a phenomenon in which the tidal amplitude is damped and the phase delayed when tides propagate through a long, narrow channel (Byun et al., 2004; Guo et al., 2017; Stigebrandt, 1980). It is a geometric feature that often occurs in macro-tidal areas with shallow water (Byun and Wang, 2005). According to model results in Fig. 14, the tidal-choking effect was enhanced in the main branch of YE due to the land reclamation. A slight drop in the M_2 amplitude, 2 cm, occurred in the East Branch after reclamation according to the harmonic analysis of tidal elevation (Fig. 14a); the phase of M_2 was also delayed by 2° (Fig. 14b). This drop in amplitude together with the delayed phase of M_2 in this area indicates the system was more choked after reclamation.

Due to the Bernoulli Equation, the reduced water level accelerates the water flow through a choked channel (Stigebrandt, 1980). This change in tidal current was also found in the YE (Fig. 14c). After land reclamation, major axis of vertically averaged M_2 tidal current increased by over 0.1 m/s due to the enhanced tidal-choking. Previous studies also found stronger tidal-choking can generate a stronger current in choked channel: for example, tidal current in the Mokpo Coastal Zone was larger due to the enhanced tidal-choking (Byun et al., 2004); current in the Yangshan Harbour channel was increased as a consequence of stronger tidal choking after narrowing (Guo et al., 2017); and the removal of tidal flats in the Jiaozhou Bay and less mangroves in the Darwin Harbour resulted in a decreased current speed due to reduced tidal choking (Gao et al., 2014; Li et al., 2012).

The intensity of turbulent mixing is described using vertical and horizontal turbulent eddy viscosities. The enhanced tidal-choking effect leads to stronger mixing processes in the

East Branch: both vertical and horizontal eddy viscosities were increased post-reclamation (Figs.14d, e). This provides an explanation to the dramatic change in the REE sedimentation around 1975: the larger vertical mixing hindered the settling of suspended particles in the water column, enhanced the mixing of the different sediments (from multiple sources) before they deposit to the seabed, resulting in a more homogeneous local deposits on the seabed (as discussed in Section 4.1). The slightly larger post-reclamation horizontal mixing caused a stronger horizontal dispersion of sediments in the water, which also contributed to the homogeneity of sediments in the East Branch.

5.2 Variations of suspended sediment transport

In order to understand the transport of suspended sediments between the estuary and surrounding shallow waters, the profiles of SSC and net suspended-sediment transport across the estuary entrance line (Fig. 1) was shown in Fig. 15. For both experiments, larger SSC were found at bottom in the west side of the entrance, near the Middle River (Fig. 15a). This bottom patch of higher SSC became larger post-reclamation in Experiment 2. The net sediment flux was seaward at the western end of the cross-section and landward at the eastern part. The overall direction of the net sediment flux was landward. However, this landward flux was reduced post-reclamation, especially near the Middle River (Fig. 15f).

The sediment flux across the entrance indicated that the estuary experienced erosion on its west side and siltation on the east. However, the intensity of erosion increased significantly across the whole entrance after land reclamation. Estuaries tend to be a sink for cohesive, fine sediments, especially those with weak dynamic environments (Cundy et al., 2003). But in a macro-tidal estuary like the YE, sediments can be easily remobilized by strong currents. Therefore, dramatic changes in tidal dynamics may induce a “sink-to-source” transformation of the YE. The reduced landward sediment flux in the YE implies that the estuary may experience more erosion instead of siltation and shift from a sediment sink to a

source if more land is reclaimed in the future.

To investigate further the main physical mechanisms driving this change, the net sediment flux was decomposed using Eq. (11). Figure 16a displays the decomposed sediment flux at sites K1 and K12 (Fig.1) in Experiments 1 and 2. Tidal pumping (terms T_3, T_4 and T_5) was the dominant mechanism for sediment transport at these two sites, following by sediment flux generated by Eulerian-residual current (T_1). As the estuary was vertically well-mixed, sediment flux induced by vertical circulation (T_6 and T_7) at the two sites was negligible in both scenarios.

The direction of sediment transport was consistently landward at K1 and K12 (Fig. 16b). However, the dominant landward contribution from tidal pumping decreased significantly post-reclamation, consistent with the seaward advective sediment flux slightly increased. Tidal pumping effect decreased because of the reduced flood dominance (Section 4.2.1, Fig. 11). And the seaward flux (the Lagrangian flux in Fig. 16b) was enhanced due to the larger seaward residual currents (river flows concentrated more in the main branch post-reclamation whereas they can be transported through the lateral Yingmen Channel before). As a consequence of these changes, the total landward transport of sediments at these sites decreased by more than 50% after land reclamation.

Previous studies proposed that the YE is a sink for sediments, with resuspended sediments moving landward at the entrance line (Gao et al., 2004, 2003; Liu et al., 2013). Results from the sediment model in this study confirmed this hypothesis. However, although general tendency of SSC transport has always been landward, the degree of this landward transport decreased significantly after the land reclamation as discussed in this section.

5.3 Changes in sediment sources

As discussed in Section 4.1, the property of deposits at the two sites (K1 and K12 in

Fig. 1) changed significantly and became similar after 1975. To investigate this change in sediments in the East Branch area post-reclamation, particle resuspension and tracking simulations were conducted using TrackMPD (Section 3.3.3). Fig. 17 shows the trajectories of these simulated particles.

Fluvial particles released upstream (RN in Fig. 17) could be transported through the Yingmen Channel and West River before reclamation but distributed mainly in the East Branch afterwards. The fluvial particles therefore contributed significantly more to the estuarine deposits after reclamation, corresponding to the increased seaward sediment flux discussed in Section 5.2.

A similar pattern was also found in particles from the middle region of the East Branch (representing local resuspended particles; LR in Fig. 17). Due to the stronger mixing post-reclamation, the trajectories of the LR particles were more spread out.

The particles released from shallow water in the NYS (SW in Fig. 17) did not show any obvious change in their trajectories. These particles did reach further north to the inner estuary after reclamation, but still had a relatively low probability of being transported to K1 and K12. A previous study using indicative minerals for provenance tracking treated this particular shallow-water area as a sediment source (termed “neritic sediments” in their study), together with the fluvial source (Liu et al., 2013). According to our model results, there was a tendency for these particles to accumulate around the Xin Island before reclamation. However, they were more distributed in the shallow water away from the estuary afterwards.

Pre-reclamation, particles released from WR can be washed away into the NYS, whereas it generally remained around WR post-reclamation. Additionally, particles from the fluvial area (RN) reached WR before reclamation but no longer transported to this area afterwards. These results suggested the sediment source of WR changed from fluvial materials to local deposits after land reclamation. The reason for this phenomenon is that the

West Channel (WR in Fig.17) was transformed from a main water outlet into an abandoned tidal waterway over a relatively short time. After reclamation, the WR area received only a very small amount of river discharge and turned into a gulf-like environment. Thus, deposits here were mainly from local resuspended sediments controlled by tides. Before the expansion of the islands in the early 1970s, the bulk of these local sediments were from fluvial input. A previous study also found that the deposits in the West Channel were old fluvial materials (Liu et al., 2013). This would provide an explanation to why the sediments in the East Branch at K1 and K12 after reclamation had similar REE properties to the surface sediments from the Liaodong muddy coast (Section C in Fig.1, which is near WR).

In terms of particles released from Western Korean Bay (WK in Fig.17), the trajectories of these particles covered a larger part of the estuary before reclamation but were restricted to a smaller area afterwards.

Several conclusions can be drawn from these particle-tracking results. **(1)** Before reclamation, site K1 mainly received particles from the Western Korean Bay region; particles from other areas did not reach K1. Sediments at K12 were multiple sources, which contained mainly fluvial materials (from RN), partly local resuspended particles from the East Branch (LR) and a small amount of neritic sediments (SW). **(2)** After reclamation, the bulk of the sediments at both K1 and K12 were derived predominantly from two sources: fluvial input (from RN); and local resuspended sediments from main-branch deposits (LR).

These conclusions help to explain the REE results in Section 4.1: bulk of the deposits at K1 had a distinct REE property before reclamation, suggesting a single sediment input from the Western Korean Bay. At K12 before reclamation, sediments had diverse REE properties, corresponding to the multiple sediment sources implied by the particle-tracking results. After land reclamation, deposits at both K1 and K12 became similar to those from Section C (the WR area; Fig. 2a) because they have a more common composition (with

735 sediments from RN and LR).

736 Essentially, after land reclamation, the estuarine main branch (the East Branch)
737 received more materials from fluvial inputs due to the increased seaward flux caused by
738 reduced flood dominance; the deposits became more homogeneous, with a common
739 composition that contains more fluvial and local resuspended sediments as a result of
740 stronger mixing; particles from the Western Korean Bay no longer transported to the inner
741 estuary.

742 6 Conclusion

743 This study firstly examined the historical variations in rare-earth element (REE)
744 sedimentation in the Yalu River Estuary (YE). The REE records in two cores (K1 and K12)
745 demonstrated there was a dramatic change in sedimentation in the YE around the year 1975.
746 Results indicated that sediment property in the main branch has changed from diverse to
747 homogenous after 1975.

748 Then a 3D hydrodynamic-sediment model was established in the YE for the first time
749 to explore the structure of the estuarine dynamics pre- and post-reclamation. Model results
750 showed that the local hydrodynamics changed significantly after the land reclamation: (1) the
751 magnitude of the tidal currents during both spring and neap tide increased; (2) the degree of
752 the flood dominance in the main branch was reduced; (3) tidal-choking in the estuary was
753 found to be enhanced; and (4) the intensity of turbulent mixing became stronger.

754 The varying hydrodynamics leaded to changes in sediment transport post-reclamation:
755 (1) the SSC in the main branch of YE increased greatly by 140 mg/L; (2) the difference
756 between surface and bottom SSC also increased; (3) there was a larger horizontal SSC
757 gradient between the inner and outer estuary; (4) although the net suspended sediment flux
758 remained landward, this landward transport has been weakened after reclamation; and (5) the
759 dominant landward sediment flux caused by tidal pumping decreased significantly, with a

slightly increase in the seaward Lagrangian flux. These changes in sediment transport showed that erosion in the estuary was enhanced after the reclamation, which may change the estuary from a sediment sink to a source if the reclamation continues.

Simulations from a newly developed Lagrangian 3-D particle resuspension and tracking model demonstrated that the sediment source of the estuary altered after reclamation as well: (1) site K1 at the mouth of the estuary received more sediment particles from the Western Korean Bay before the reclamation, whereas K12 received particles from multiple areas; (2) the source area of sediments at the two sites and in the East Branch area became similar post-reclamation, with most particles from the river and local resuspension. These results presented an explanation to the previous results found in the REE sediment records: the main branch of the estuary received more fluvial sediments after 1975 due to the stronger seaward flux caused by the reduced flood dominance; and sediments at K1 and K12 showed homogeneity after 1975, with a common composition as a result of the stronger mixing.

Results from this study demonstrates the possibility of a “source-sink” shift in a medium-scale estuary after a large-scale land reclamation. This study also contributes to a better understanding of the link between changes in sediment source and their relationship with suspended-sediment transport. Furthermore, this study gives an approach to future study of a medium-to-long term estuarine sedimentation process by combining numerical simulations and geochemical results of sedimentology.

Acknowledgments

This study was supported by the Natural Science Foundation of China (No. 41876087), and we thank Eastern Liaoning University for providing the sediment core sample data. We acknowledge Nanjing University and the Yalu Park Hydrology Station for supplying field measurements for water level and currents in the study area. This manuscript benefits from editorial help from Peter McIntyre from UNSW Canberra. This study is also supported by the

National Computational Infrastructure National Facility at the Australian National University, which provided computational resources. This is Publication No. 77 of the Sino-Australian Research Centre for Coastal Management at UNSW Canberra, Australia. The TrackMPD version 1.2 proposed in this study with the resuspension module and time-dependent K_z can be found at https://github.com/IJalonRojas/TrackMPD.

Competing interest

The authors declare no competing interest.

Reference

Appleby, P.G., 1997. Sediment records of fallout radionuclides and their application to studies of sediment-water interactions. Water, Air Soil Pollut. 99 99, 573–585.

Ariathurai, R., Krone, R.B., 1977. Mathematical modeling of sediment transport in estuaries, in: Estuarine Processes. Elsevier, pp. 98–106. https://doi.org/10.1016/B978-0-12-751802-2.50015-1

Brenon, I., Hir, P. Le, 1999. Modelling the Turbidity Maximum in the Seine Estuary (France): Identification of Formation. Simulation 525–544.

Brito, P., Prego, R., Mil-Homens, M., Caçador, I., Caetano, M., 2018. Sources and distribution of yttrium and rare earth elements in surface sediments from Tagus estuary, Portugal. Sci. Total Environ. 621, 317–325. https://doi.org/10.1016/j.scitotenv.2017.11.245

Byun, D.S., Wang, X.H., 2005. The effect of sediment stratification on tidal dynamics and sediment transport patterns. J. Geophys. Res. C Ocean. 110, 1–16. https://doi.org/10.1029/2004JC002459

Byun, D.S., Wang, X.H., Holloway, P.E., 2004. Tidal characteristic adjustment due to dyke and seawall construction in the Mokpo Coastal Zone, Korea. Estuar. Coast. Shelf Sci. 59, 185–196. https://doi.org/10.1016/j.ecss.2003.08.007

Chakraborti, R.K., Kaur, J., 2014. Noninvasive measurement of particle-settling velocity and comparison with Stokes' Law. J. Environ. En- gineering 140. https://doi.org/10.1061/EE.1943-7870.0000790

Chen, C., Beardsley, R., Cowles, G., Qi, J., Lai, Z., Gao, G., Stuebe, D., Xu, Q., Xue, P., Ge, J., Hu, S., Ji, 2013. An unstructured grid, Finite-Volume Coastal Ocean Model FVCOM -- User Manual. Tech. Rep., SMAST/UMASSD-13-0701, Sch. Mar. Sci. Technol., Univ. Mass. Dartmouth, New Bedford. C, 416 pp. https://doi.org/10.1017/CBO9781107415324.004

Chen, C., Liu, H., Beardsley, R., 2003. An unstructured grid, finite-volume, three-dimensional, primitive equations ocean model: application to coastal ocean and estuaries. J. Atmos. Ocean. Technol. 20, 159–186.

Chen, X., Li, T., Zhang, X., Li, R., 2013. A Holocene Yalu River-derived fine-grained deposit in the southeast coastal area of the Liaodong Peninsula. Chinese J. Oceanol. Limnol. 31, 636–647. https://doi.org/10.1007/s00343-013-2087-1

Cheng, Y., 2007. Estuary landform's formation and evolution of the YaLu River. Northeast Normal University.

Cheng, Z., Wang, X., Paull, D., Gao, J., 2016. Application of the Geostationary Ocean Color Imager to Mapping the Diurnal and Seasonal Variability of Surface Suspended Matter in a Macro-Tidal Estuary. Remote Sens. 8, 244. https://doi.org/10.3390/rs8030244

Cheng, Z., Wang, X.H., Rojas, I.J., Liu, Y., 2019. Reconstruction of sedimentation changes under anthropogenic influence in a medium-scale estuary based on a decadal chronological framework. Estuar. Coast. Shelf Sci. 106295. https://doi.org/10.1016/j.ecss.2019.106295

Collias, N.E., 1943. Statistical analysis of factors which make for success in initial encounters between hens. Am. Nat. 77, 519–538.

835 Cundy, A.B., Croudace, I.W., Cearreta, A., Irabien, M.J., 2003. Reconstructing historical
836 trends in metal input in heavily-disturbed, contaminated estuaries: Studies from Bilbao,
837 Southampton Water and Sicily. Appl. Geochemistry 18, 311–325.
838 https://doi.org/10.1016/S0883-2927(02)00127-0
839 Dijkstra, Y.M., Schuttelaars, H.M., Schramkowski, G.P., 2019. A Regime Shift From Low to
840 High Sediment Concentrations in a Tide-Dominated Estuary. Geophys. Res. Lett. 46,
841 4338–4345. https://doi.org/10.1029/2019GL082302
842 Dyer, K.R., 1997. Estuaries: a physical introduction. 2nd edition, John Wiley & Sons.
843 https://doi.org/ISBN 0-471-9741-4
844 Gao, G.D., Wang, X.H., Bao, X.W., 2014. Land reclamation and its impact on tidal dynamics
845 in Jiaozhou Bay, Qingdao, China. Estuar. Coast. Shelf Sci. 151, 285–294.
846 https://doi.org/10.1016/j.ecss.2014.07.017
847 Gao, G.D., Wang, X.H., Song, D., Bao, X., Yin, B.S., Yang, D.Z., Ding, Y., Li, H., Hou, F.,
848 Ren, Z., 2018. Effects of wave-current interactions on suspended-sediment dynamics
849 during strong wave events in Jiaozhou Bay, Qingdao, China. J. Phys. Oceanogr. 1053–
850 1078. https://doi.org/10.1175/jpo-d-17-0259.1
851 Gao, J., Gao, S., Cheng, Y., Dong, L., Zhang, J., 2004. Formation of Turbidity Maxima in the
852 Yalu River Estuary, China. J. Coast. Res. 134–146.
853 Gao, J., Li, J., Wang, H., Bai, F. long, Cheng, Y., Wang, Y. ping, 2012. Rapid changes of
854 sediment dynamic processes in Yalu River Estuary under anthropogenic impacts. Int. J.
855 Sediment Res. 27, 37–49. https://doi.org/10.1016/S1001-6279(12)60014-6
856 Gao, J., Li, J., Wang Harry, V., Wang, Y., Wang, Z., Bai, F., Gao, S., Cheng, Y., 2009.
857 Distribution and their pollution assessment of heavy metals in the sediments of the Yalu
858 River Estuary and its adjacent coastal waters. Acta Oceanol. Sin. -English Ed. 28, 12–
859 23.

Gao, J., Gao, S., Cheng, Y., Dong, L.X., Zhang, J., 2003. Sediment transport in Yalu River estuary. Chinese Geogr. Sci. 13, 157–163. https://doi.org/10.1007/s11769-003-0010-y

Gao, S., Wang, D., Yang, Y., Zhou, L., Zhao, Y., Gao, W., Han, Z., Yu, Q., Li, G., 2016. Holocene sedimentary systems on a broad continental shelf with abundant river input: Process-product relationships. Geol. Soc. Spec. Publ. 429, 223–259. https://doi.org/10.1144/SP429.4

Ge, J., Chen, C., Qi, J., Ding, P., Beardsley, R.C., 2012. A dike-groyne algorithm in a terrain-following coordinate ocean model (FVCOM): Development, validation and application. Ocean Model. 47, 26–40. https://doi.org/10.1016/j.ocemod.2012.01.006

Glenn, S.M., Grant, W.D., 1987. A suspended sediment stratification correction for combined wave and current flows. J. Geophys. Res. 92, 8244–8264. https://doi.org/10.1029/JC092iC08p08244

Guo, W., Wang, X.H., Ding, P., Ge, J., Song, D., 2017. A system shift in tidal choking due to the construction of Yangshan Harbour, Shanghai, China. Estuar. Coast. Shelf Sci. 206, 49–60. https://doi.org/10.1016/j.ecss.2017.03.017

Hannigan, R., Dorval, E., Jones, C., 2010. The rare earth element chemistry of estuarine surface sediments in the Chesapeake Bay. Chem. Geol. 272, 20–30. https://doi.org/10.1016/j.chemgeo.2010.01.009

Hathorne, E.C., Stichel, T., Brück, B., Frank, M., 2014. Rare earth element distribution in the Atlantic sector of the Southern Ocean: The balance between particle scavenging and vertical supply. Mar. Chem. 177, 157–171. https://doi.org/10.1016/j.marchem.2015.03.011

Jalón-Rojas, I., Schmidt, S., Sottolichio, A., 2015. Turbidity in the fluvial Gironde Estuary (southwest France) based on 10-year continuous monitoring: Sensitivity to hydrological conditions. Hydrol. Earth Syst. Sci. 19, 2805–2819. https://doi.org/10.5194/hess-19-

2805-2015

Jalón-Rojas, I., Sottolichio, A., Hanquiez, V., Fort, A., Schmidt, S., 2018. To what extent multidecadal changes in morphology and fluvial discharge impact tide in a convergent (turbid) tidal river. J. Geophys. Res. Ocean. 123, 1–18. https://doi.org/10.1002/2017JC013466

Jalón-Rojas, I., Wang, X.H., Fredj, E., 2019. A 3D numerical model to Track Marine Plastic Debris (TrackMPD): Sensitivity of microplastic trajectories and fates to particle dynamical properties and physical processes. Mar. Pollut. Bull. 141, 256–272. https://doi.org/10.1016/j.marpolbul.2019.02.052

Ji, Z.G., 2006. Hydrodynamics and water quality - Modelling rivers, lakes and estuaries.

Jung, H.S., Lim, D., Choi, J.Y., Yoo, H.S., Rho, K.C., Lee, H.B., 2012. Rare earth element compositions of core sediments from the shelf of the South Sea, Korea: Their controls and origins. Cont. Shelf Res. 48, 75–86. https://doi.org/10.1016/j.csr.2012.08.008

Lackey, T., Macdonald, N., 2007. The Particle Tracking Model : Description and Processes. Proc. XVIII World Dredg. Congr. 551–566.

Lane, A., 2005. Development of a Lagrangian sediment model to reproduce the bathymetric evolution of the Mersey Estuary. Ocean Dyn. 55, 541–548. https://doi.org/10.1007/s10236-005-0011-8

Leybourne, M.I., Johannesson, K.H., 2008. Rare earth elements (REE) and yttrium in stream waters, stream sediments, and Fe-Mn oxyhydroxides: Fractionation, speciation, and controls over REE + Y patterns in the surface environment. Geochim. Cosmochim. Acta 72, 5962–5983. https://doi.org/10.1016/j.gca.2008.09.022

Li, L., Wang, X.H., Andutta, F., Williams, D., 2014. Effects of mangroves and tidal flats on suspended-sediment dynamics: Observational and numerical study of Darwin Harbour, Australia. J. Geophys. Res. Ocean. 119, 5854–5873.

https://doi.org/10.1002/2014JC009987

Li, L., Wang, X.H., Williams, D., Sidhu, H., Song, D., 2012. Numerical study of the effects of mangrove areas and tidal flats on tides: A case study of Darwin Harbour, Australia. J. Geophys. Res. Ocean. 117, 1–12. https://doi.org/10.1029/2011JC007494

Li, Y., Li, A.C., Huang, P., Xu, F.J., Zheng, X.F., 2014. Clay minerals in surface sediment of the north Yellow Sea and their implication to provenance and transportation. Cont. Shelf Res. 90, 33–40. https://doi.org/10.1016/j.csr.2014.01.020

Lim, D., Jung, H.S., Choi, J.Y., 2014. REE partitioning in riverine sediments around the Yellow Sea and its importance in shelf sediment provenance. Mar. Geol. 357, 12–24. https://doi.org/10.1016/j.margeo.2014.07.002

Liu, Y., 2016. Provenance tracking of macroelements in surface sediments from the Yalu River estuary, China. Toxicol. Environ. Chem. 98, 313–326. https://doi.org/10.1080/02772248.2015.1123477

Liu, Y., Cheng, Y., Li, H., Liu, J., Zhang, C., Zhang, L., Zheng, C., Gao, J., 2013. Provenance tracing of indicative minerals in sediments of the Yalu River Estuary and its adjacent shallow seas. J. Coast. Res. 290, 1227–1235. https://doi.org/10.2112/JCOASTRES-D-12-00269.1

Liu, Y., Cheng, Y., Liu, J., Zhang, L., Zhang, C., Zheng, C., 2015. Provenance discrimination of surface sediments using rare earth elements in the Yalu River estuary, China. Environ. Earth Sci. 74, 3507–3517. https://doi.org/10.1007/s12665-015-4391-x

Liubartseva, S., Coppini, G., Lecci, R., Clementi, E., 2018. Tracking plastics in the Mediterranean: 2D Lagrangian model. Mar. Pollut. Bull. 129, 151–162. https://doi.org/10.1016/j.marpolbul.2018.02.019

Martins, V., Figueira, R.C.L., França, E.J., Ferreira, P.A. de L., Martins, P., Santos, J.F., Dias, J.A., Laut, L.L.M., Monge Soares, A.M., Silva, E.F. da, Rocha, F., 2012. Sedimentary

processes on the NW Iberian Continental Shelf since the Little Ice Age. Estuar. Coast. Shelf Sci. 102–103, 48–59. https://doi.org/10.1016/j.ecss.2012.03.004

Mellor, G.L., Yamada, T., 1982. Development of a turbulence closure model for geophysical fluid problems. Rev. Geophys. 20, 851–875. https://doi.org/10.1029/RG020i004p00851

Moore, R.D., Wolf, J., Souza, A.J., Flint, S.S., 2009. Morphological evolution of the Dee Estuary, Eastern Irish Sea, UK: A tidal asymmetry approach. Geomorphology 103, 588–596. https://doi.org/10.1016/j.geomorph.2008.08.003

Orani, A.M., Vassileva, E., Wysocka, I., Angelidis, M., Rozmaric, M., Louw, D., 2018. Baseline study on trace and rare earth elements in marine sediments collected along the Namibian coast. Mar. Pollut. Bull. 131, 386–395. https://doi.org/10.1016/j.marpolbul.2018.04.021

Ralston, D.K., Talke, S., Geyer, W.R., Al-Zubaidi, H.A.M., Sommerfield, C.K., 2019. Bigger Tides, Less Flooding: Effects of Dredging on Barotropic Dynamics in a Highly Modified Estuary. J. Geophys. Res. Ocean. 124, 196–211. https://doi.org/10.1029/2018JC014313

Shi, Y., Gao, J.H., Sheng, H., Du, J., Jia, J.J., Wang, Y.P., Li, J., Bai, F.L., Chen, Y.N., 2018. Cross-front sediment transport induced by quick oscillation of the Yellow Sea Warm Current: Evidence from the sedimentary record. Geophys. Res. Lett. 1–9. https://doi.org/10.1029/2018GL080751

Shynu, R., Rao, V.P., Parthiban, G., Balakrishnan, S., Narvekar, T., Kessarkar, P.M., 2013. REE in suspended particulate matter and sediment of the Zuari estuary and adjacent shelf, western India: Influence of mining and estuarine turbidity. Mar. Geol. 346, 326–342. https://doi.org/10.1016/j.margeo.2013.10.004

Smagorinsky, J., 1963. General circulation experiments with the primitive equations. Mon. Weather Rev. 91, 99–164.

960 Song, D., Wang, X.H., 2013. Suspended sediment transport in the Deepwater Navigation
961 Channel, Yangtze River Estuary, China, in the dry season 2009: 2. Numerical
962 simulations. J. Geophys. Res. Ocean. 118, 5568–5590.
963 https://doi.org/10.1002/jgrc.20411
964 Song, D., Wang, X.H., Kiss, A.E., Bao, X., 2011. The contribution to tidal asymmetry by
965 different combinations of tidal constituents. J. Geophys. Res. Ocean. 116, 1–12.
966 https://doi.org/10.1029/2011JC007270
967 Song, D., Wang, X.H., Zhu, X., Bao, X., 2013. Modeling studies of the far-field effects of
968 tidal flat reclamation on tidal dynamics in the East China Seas. Estuar. Coast. Shelf Sci.
969 133, 147–160. https://doi.org/10.1016/j.ecss.2013.08.023
970 Song, H., Shin, W.J., Ryu, J.S., Shin, H.S., Chung, H., Lee, K.S., 2017. Anthropogenic rare
971 earth elements and their spatial distributions in the Han River, South Korea.
972 Chemosphere 172, 155–165. https://doi.org/10.1016/j.chemosphere.2016.12.135
973 Song, Y.H., Choi, M.S., 2009. REE geochemistry of fine-grained sediments from major rivers
974 around the Yellow Sea. Chem. Geol. 266, 337–351.
975 https://doi.org/10.1016/j.chemgeo.2009.06.019
976 Soulsby, R.L., Dyer, K.R., 1981. The Form of the Near-Bed Velocity Profile in a Tidally
977 Accelerating Flow. J. Geophys. Res. 86, 8067–8074.
978 Souza, A.J., Lane, A., 2013. Effects of freshwater inflow on sediment transport. J. Oper.
979 Oceanogr. 6, 27–31. https://doi.org/10.1080/1755876X.2013.11020143
980 Stigebrandt, A., 1980. Some aspects of tidal interaction with fjord constrictions. Estuar.
981 Coast. Mar. Sci. 11, 151–166. https://doi.org/10.1016/S0302-3524(80)80038-7
982 Szmytkiewicz, A., Zalewska, T., 2014. Sediment deposition and accumulation rates
983 determined by sediment trap and 210Pb isotope methods in the Outer Puck Bay (Baltic
984 Sea). Oceanologia 56, 85–106. https://doi.org/10.5697/oc.56-1.085

985 Um, I. kwon, Choi, M.S., Bahk, J.J., Song, Y.H., 2013. Discrimination of sediment
986 provenance using rare earth elements in the ulleung basin, east/japan sea. Mar. Geol.
987 346, 208–219. https://doi.org/10.1016/j.margeo.2013.09.007
988 Van Maren, D.S., Oost, A.P., Wang, Z.B., Vos, P.C., 2016. The effect of land reclamations and
989 sediment extraction on the suspended sediment concentration in the Ems Estuary. Mar.
990 Geol. 376, 147–157. https://doi.org/10.1016/j.margeo.2016.03.007
991 Van Maren, D.S., van Kessel, T., Cronin, K., Sittoni, L., 2015. The impact of channel
992 deepening and dredging on estuarine sediment concentration. Cont. Shelf Res. 95, 1–14.
993 https://doi.org/10.1016/j.csr.2014.12.010
994 Van Rijn, L.C., Kroon, A., 1993. Sediment Transport by Currents and Waves, in: Coastal
995 Engineering 1992. American Society of Civil Engineers, New York, NY, pp. 2613–2628.
996 https://doi.org/10.1061/9780872629332.199
997 Wang, X.H., 2002. Tide-Induced Sediment Resuspension and the Bottom Boundary Layer in
998 an Idealized Estuary with a Muddy Bed. J. Phys. Oceanogr. 32, 3113–3131.
999 https://doi.org/10.1175/1520-0485(2002)032<3113:TISRAT>2.0.CO;2
1000 Williams, J., Lee, G. hong, Shin, H.J., Dellapenna, T., 2015. Mechanism for sediment
1001 convergence in the anthropogenically altered microtidal Nakdong Estuary, South Korea.
1002 Mar. Geol. 369, 79–90. https://doi.org/10.1016/j.margeo.2015.08.004
1003 Winterwerp, J.C., Wang, Z.B., Van Braeckel, A., Van Holland, G., Kösters, F., 2013. Man-
1004 induced regime shifts in small estuaries - II: A comparison of rivers. Ocean Dyn. 63,
1005 1293–1306. https://doi.org/10.1007/s10236-013-0663-8
1006 Xing, F., Wang, Y.P., Wang, H. V, 2012. Tidal hydrodynamics and fine-grained sediment
1007 transport on the radial sand ridge system in the southern Yellow Sea. Mar. Geol. 291–
1008 294, 192–210. https://doi.org/10.1016/j.margeo.2011.06.006
1009 Yang, Y., Jia, J., Zhou, L., Gao, W., Shi, B., Li, Z., Wang, Y.P., Gao, S., 2019. Human-induced

changes in sediment properties and amplified endmember differences: Possible geological time markers in the future. Sci. Total Environ. 661, 63–74. https://doi.org/10.1016/j.scitotenv.2019.01.115

Yu, Q., Wang, Y., Gao, J., Gao, S., Flemming, B., 2014. Turbidity maximum formation in a well-mixed macrotidal estuary: The role of tidal pumping. J. Geophys. Res. Ocean. 119, 7705–7724. https://doi.org/10.1002/2014JC010228

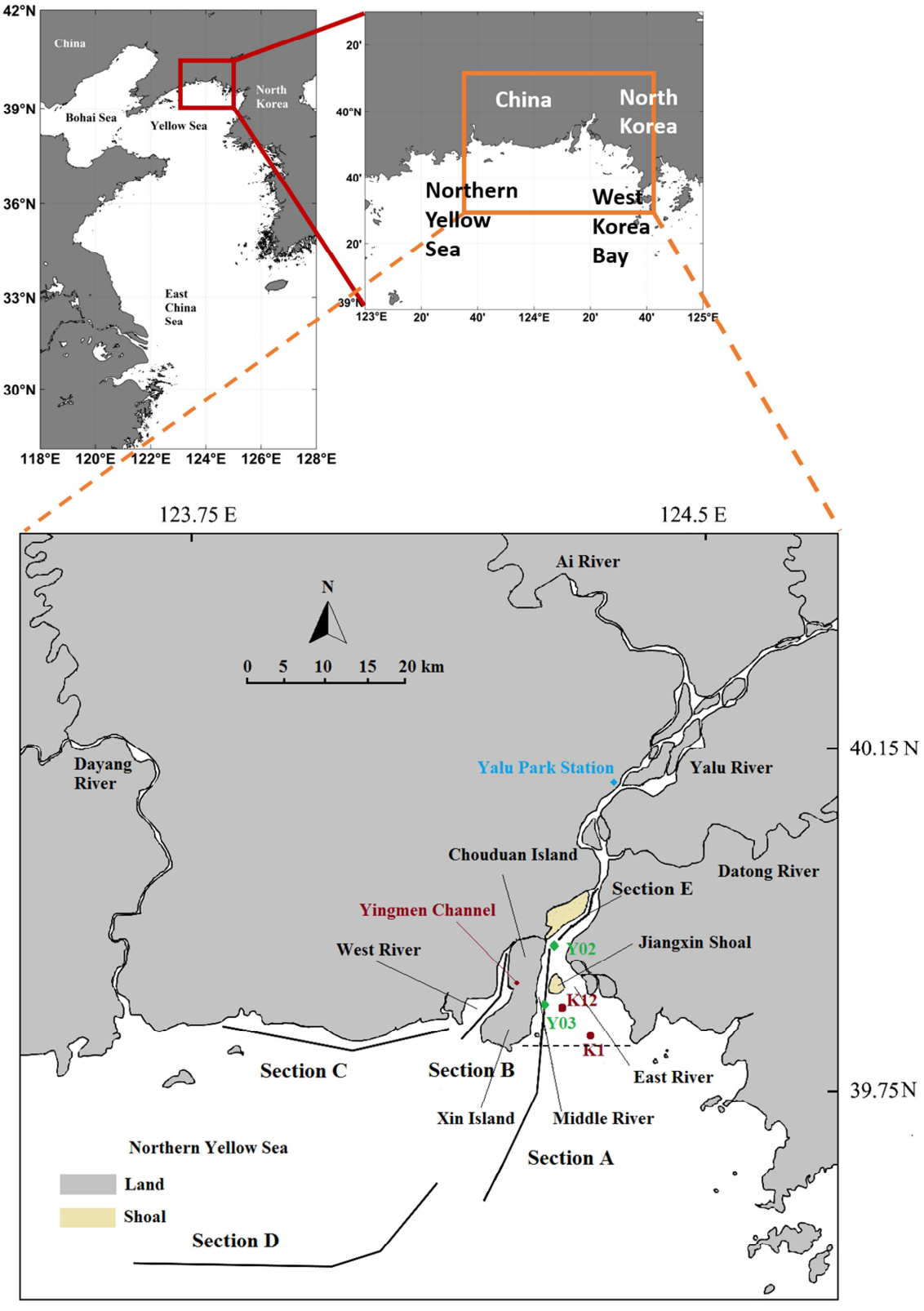
42°N
39°N
36°N
33°N
30°N
118°E
120°E
122°E
124°E
126°E
128°E
China
North Korea
Bohai Sea
Yellow Sea
East China Sea
20'
40°N
40'
20'
39°N
123°E
20'
40'
124°E
20'
40'
125°E
China
North Korea
Northern Yellow Sea
West Korea Bay
123.75 E
124.5 E
N
0 5 10 15 20 km
Ai River
Dayang River
Yalu Park Station
Yalu River
40.15 N
Chouduan Island
Datong River
Section E
Yingmen Channel
West River
Y02
Jiangxin Shoal
K12
Y03
K1
East River
Section C
Section B
39.75N
Xin Island
Middle River
Section A
Northern Yellow Sea
Land
Shoal
Section D

1017

Figure 1. Location of sampling sites around the YE and its surrounding shelf region. K1 and K12 indicate the core-sample collecting sites. Y02 and Y03 are the current-measurement sites. Yalu Park Station is the upstream hydrology station. The black dashed line shows the estuarine entrance line. Sections A, B contain surface sampling sites along the Middle River and West River, respectively. Section C contains sampling sites from the muddy coast along the Liaodong Peninsula (LP). Section D contains sites in the adjacent shallow waters outside the estuary entrance. Section E contains sites in the estuary, immediately downstream of the river.

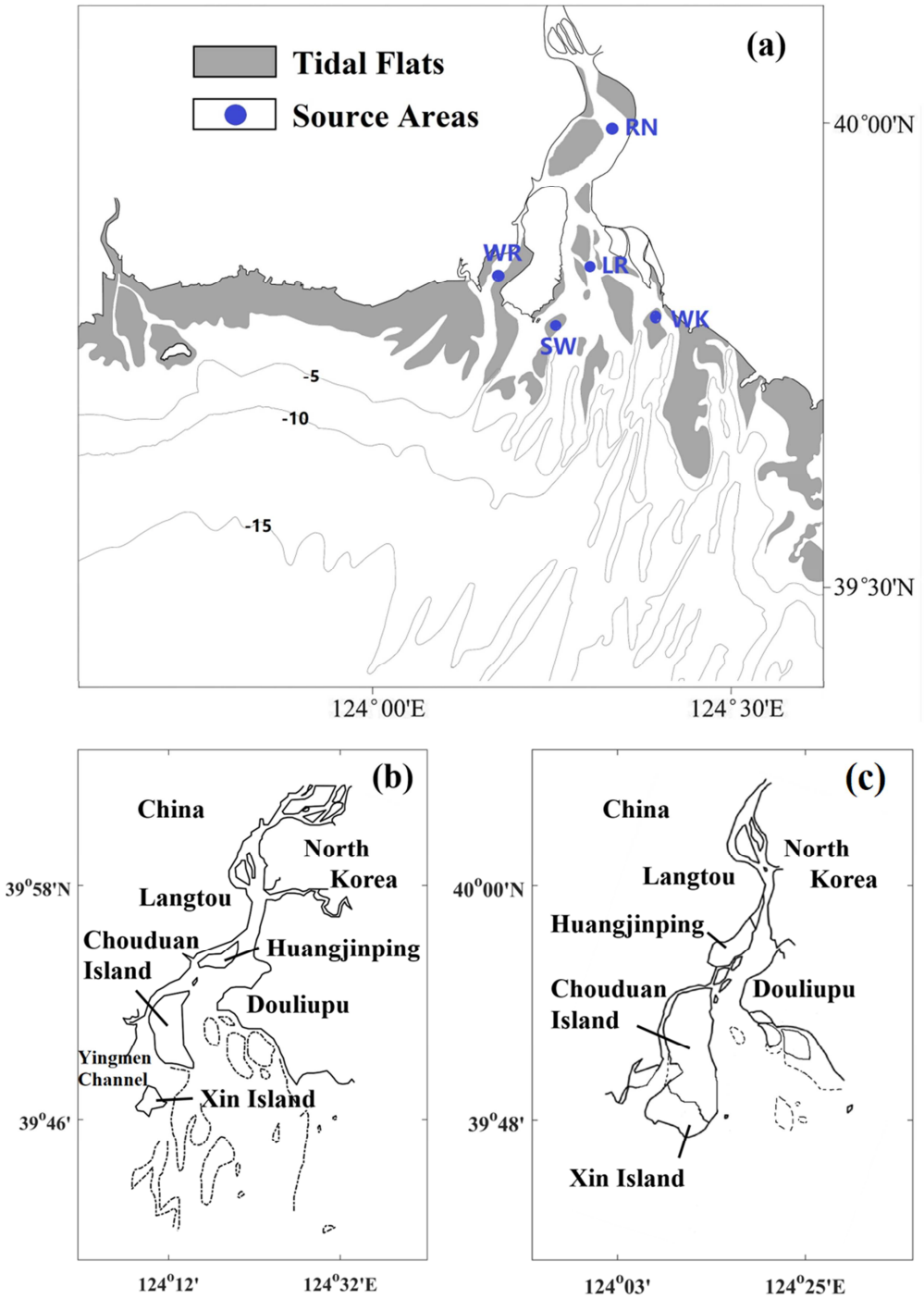
(a)
Tidal Flats
Source Areas
RN
WR
LR
WK
SW
-5
-10
-15
40°00'N
39°30'N
124°00'E
124°30'E
(b)
China
North
Korea
Langtou
Chouduan
Island
Huangjinping
Douliupu
Yingmen
Channel
Xin Island
39°58'N
39°46'
124°12'
124°32'E
(c)
China
North
Korea
Langtou
Huangjinping
Chouduan
Island
Douliupu
Xin Island
40°00'N
39°48'
124°03'
124°25'E

1026

Figure 2. **(a)** Bathymetry (black dash lines) and distribution of tidal flats (in grey) in the YE (modified from Liu et al., 2013). Points in dark blue show the potential source areas for the particle-tracking model: RN is a small area where the river flows into the estuary; WR a small area downstream of the West River; SW an area in shallow water near the entrance; WK stands for Western Korean Bay; LR is in the middle region of the estuary, with the sediment here from local resuspension in the main estuary branch. Coastline change of the YE: **(b)** coastline in 1956 **(c)** coastline in 1976 (modified from Gao et al. (2012) and Landsat image on 15 September 1976).

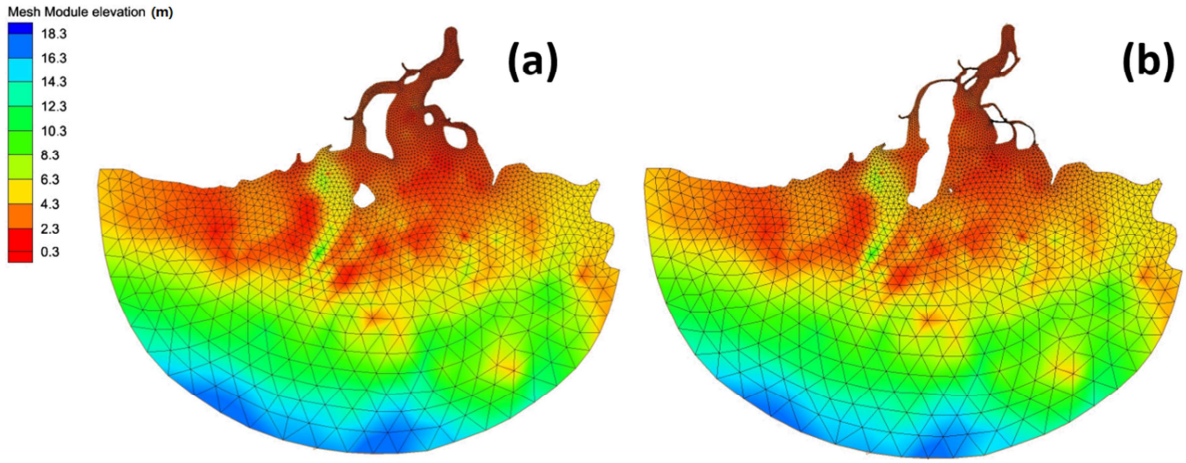

1037 **Figure 3.** Grids of the model domain for **(a)** 1956 (before land reclamation) and **(b)** 2011

1038 (after reclamation).

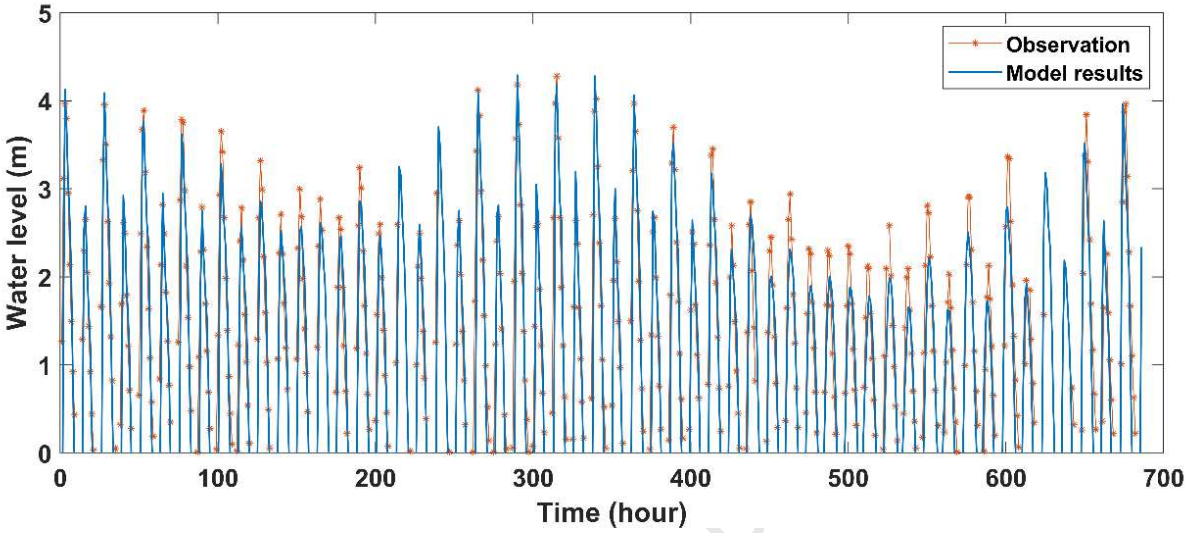

1039

Figure 4. Comparison of the measured and modelled water elevation during June 2011.

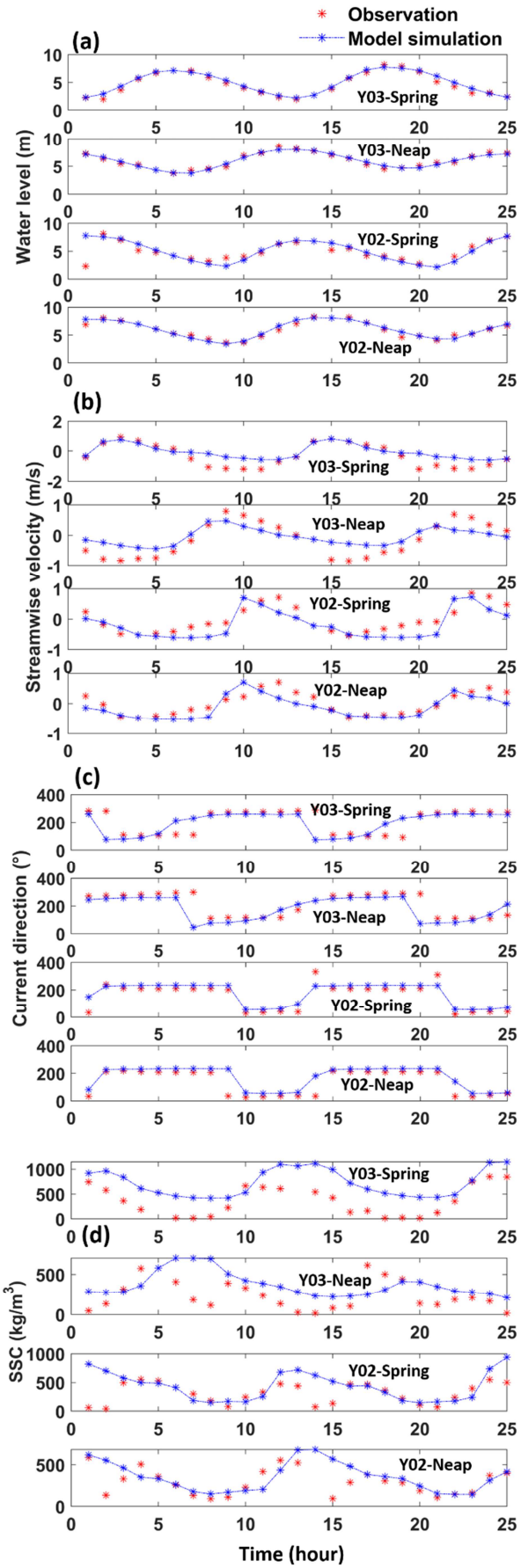
Observation
Model simulation
(a)
Water level (m)
Y03-Spring
Y03-Neap
Y02-Spring
Y02-Neap
(b)
Streamwise velocity (m/s)
(c)
Current direction (°)
(d)
SSC (kg/m3)
Time (hour)

1041

1042 **Figure 5.** Comparison of depth-averaged: **(a)** water elevation; **(b)** streamwise velocity; **(c)**
1043 current direction; and **(d)** suspended-sediment concentration between the FVCOM model
1044 results and field observations in August 2009 at Stations Y02 and Y03 during spring and neap
1045 tides.

1046

1047

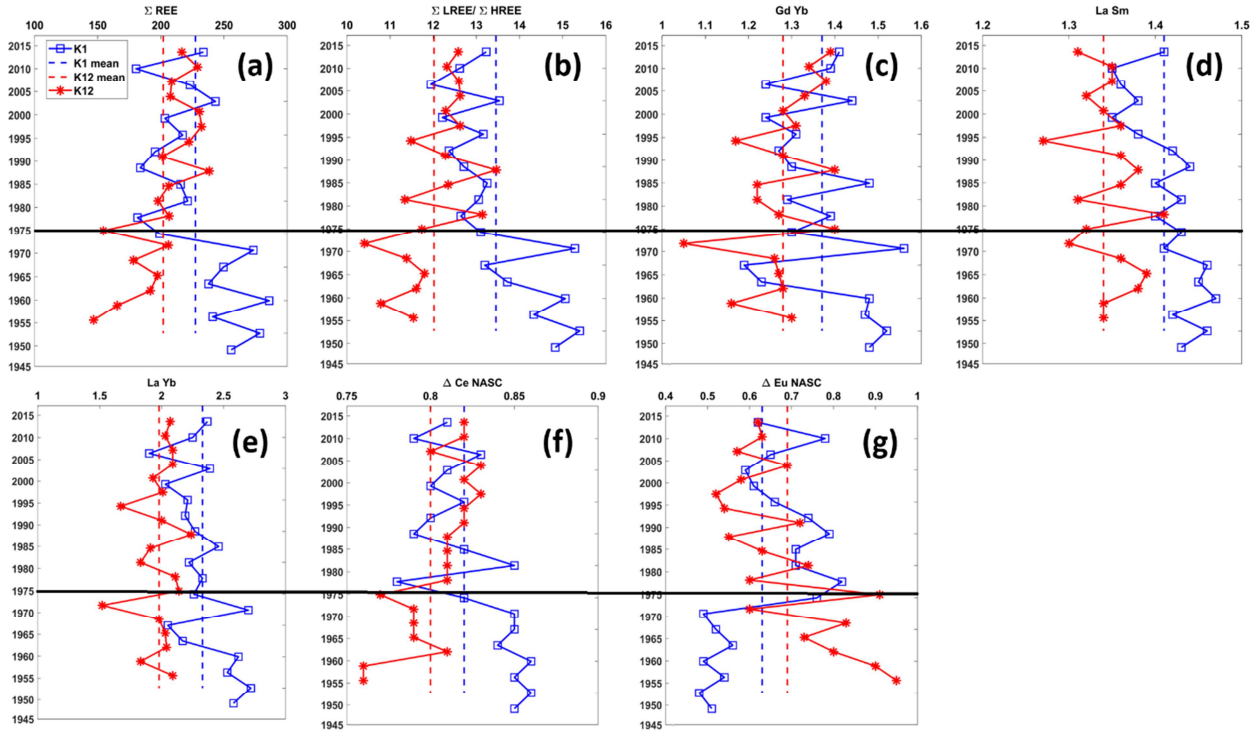

1048

1049 **Figure 6.** Profiles of **(a)** ΣREE, **(b)** ΣLREE/ΣHREE, **(c)** $(Gd/Yb)_{NASC}$, **(d)** $(La/Sm)_{NASC}$, **(e)**
1050 $(La/Yb)_{NASC}$, **(f)** δCe_{NASC} and **(g)** δEu_{NASC} in K1 and K12; dashed straight lines show the
1051 average values.

1052

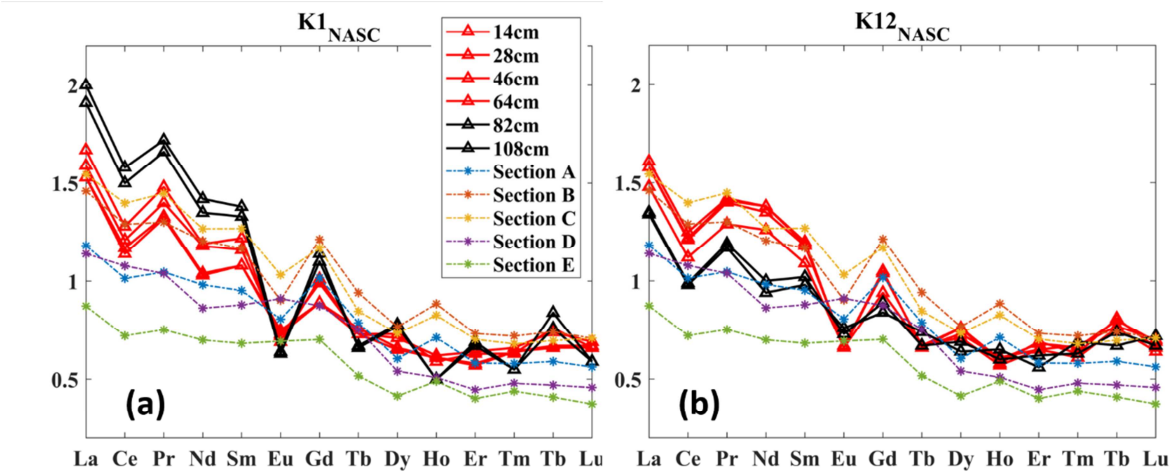

1053

1054 **Figure 7.** NASC-normalized REE patterns of K1 **(a)**, K12 **(b)** and surface samples from

1055 surrounding shallow waters. Black and red lines represent layers pre- and post-1975,

1056 respectively.

1057

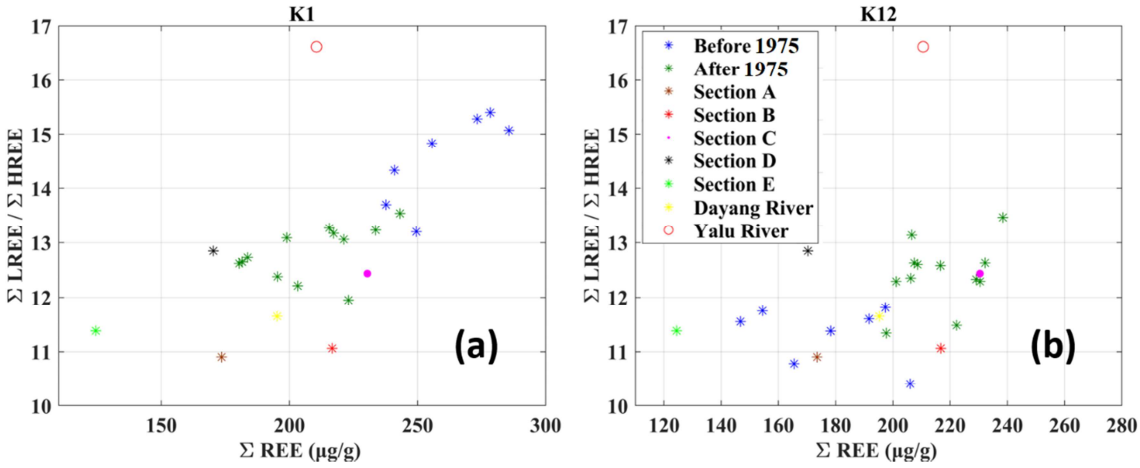

1058

Figure 8. Binary diagrams of ΣLREE/HREE and ΣREE for K1 and K12.

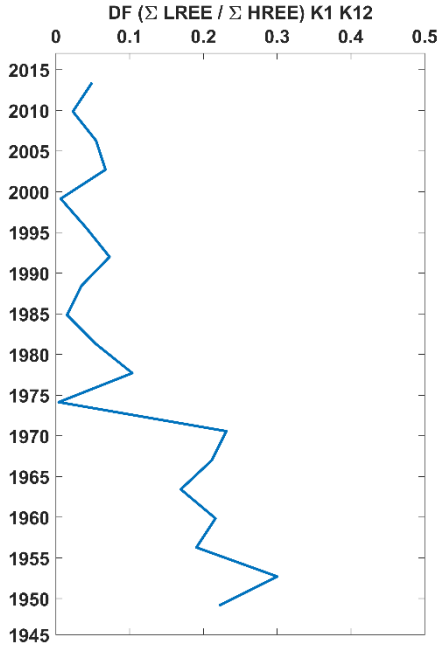

Figure 9. Vertical profile of the DF based on ΣLREE/ΣHREE between K1 and K12.

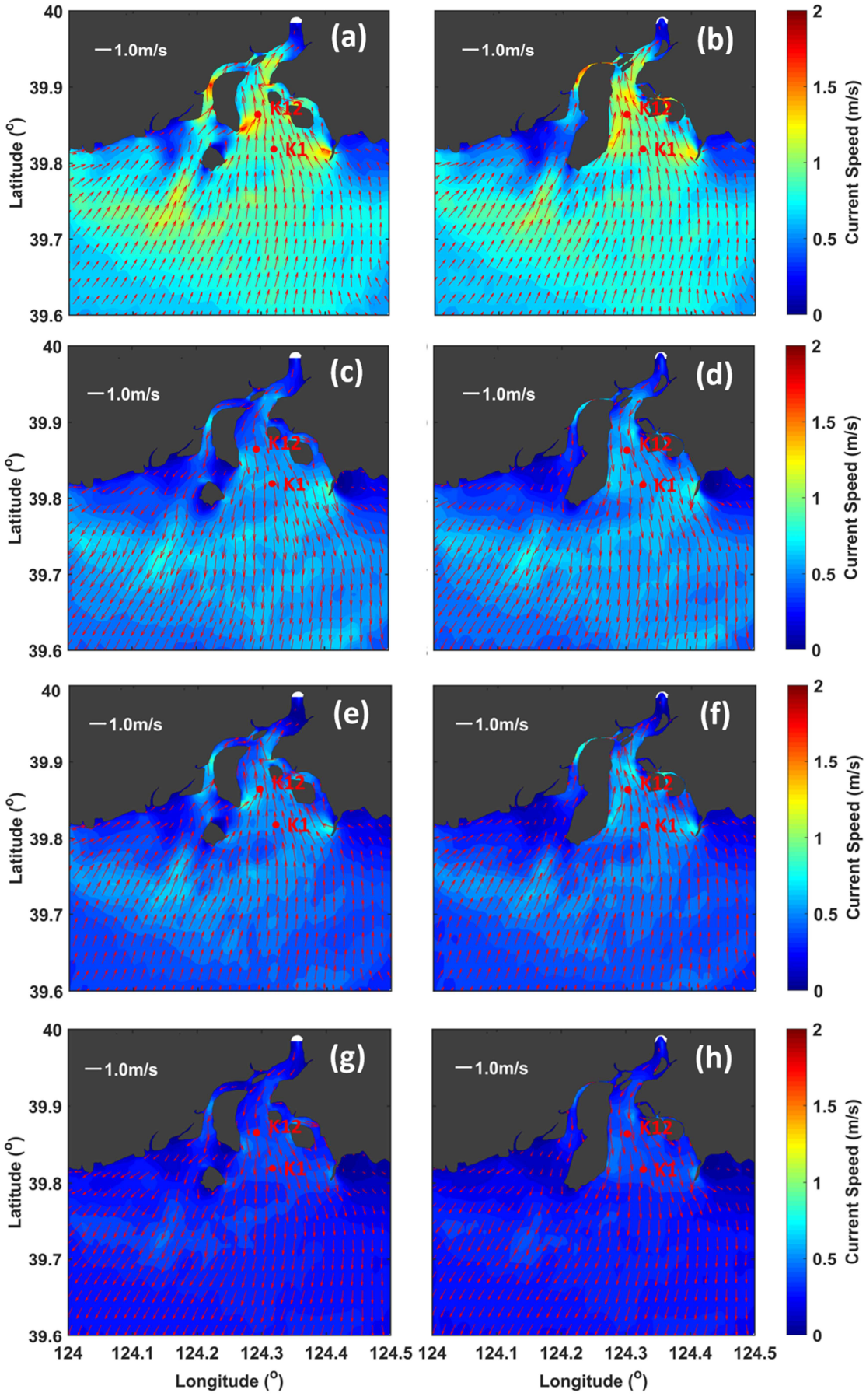
(a)
(b)
(c)
(d)
(e)
(f)
(g)
(h)
—1.0m/s
K12
K1
Latitude (°)
Longitude (°)
Current Speed (m/s)
40
39.9
39.8
39.7
39.6
124
124.1
124.2
124.3
124.4
124.5
0
0.5
1
1.5
2

1070

1071 **Figure 10.** Model depth-averaged current field during spring tide at maximum flood time **(a)**
1072 pre-reclamation (Experiment 1) and **(b)** post-reclamation (Experiment 2); **(c)** and **(d)** show
1073 the corresponding current fields at maximum ebb time. **(e, f, g, h)** as for Figs. 10(a, b, c, d)
1074 but during neap tide.

1075

1076

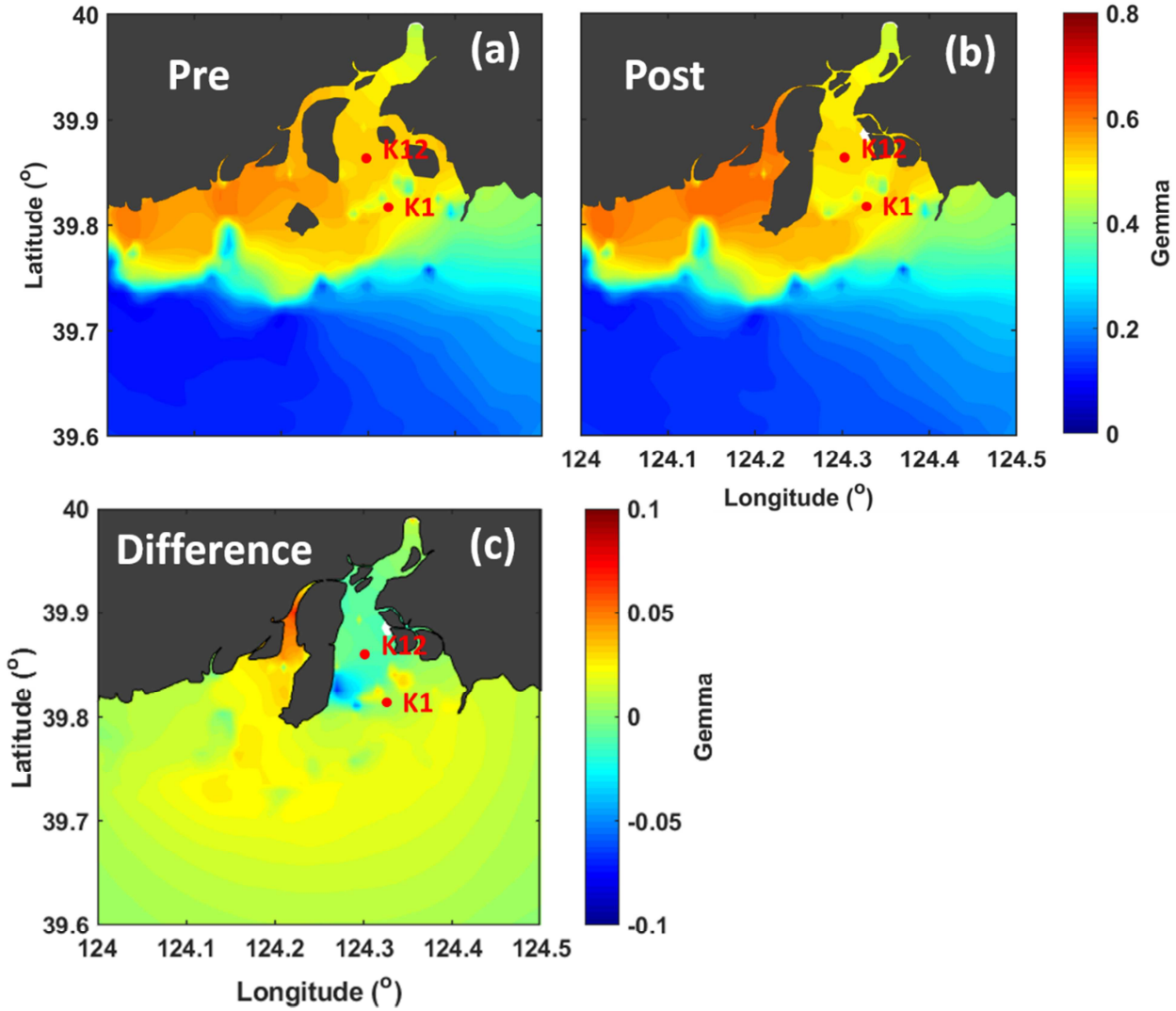

1077
1078 **Figure 11.** Model tidal asymmetry skewness field **(a)** pre-reclamation (Experiment 1) and **(b)**
1079 post-reclamation (Experiment 2); **(c)** difference in the tidal asymmetry skewness between the
1080 two experiments (Experiment 2 – Experiment 1).

1081

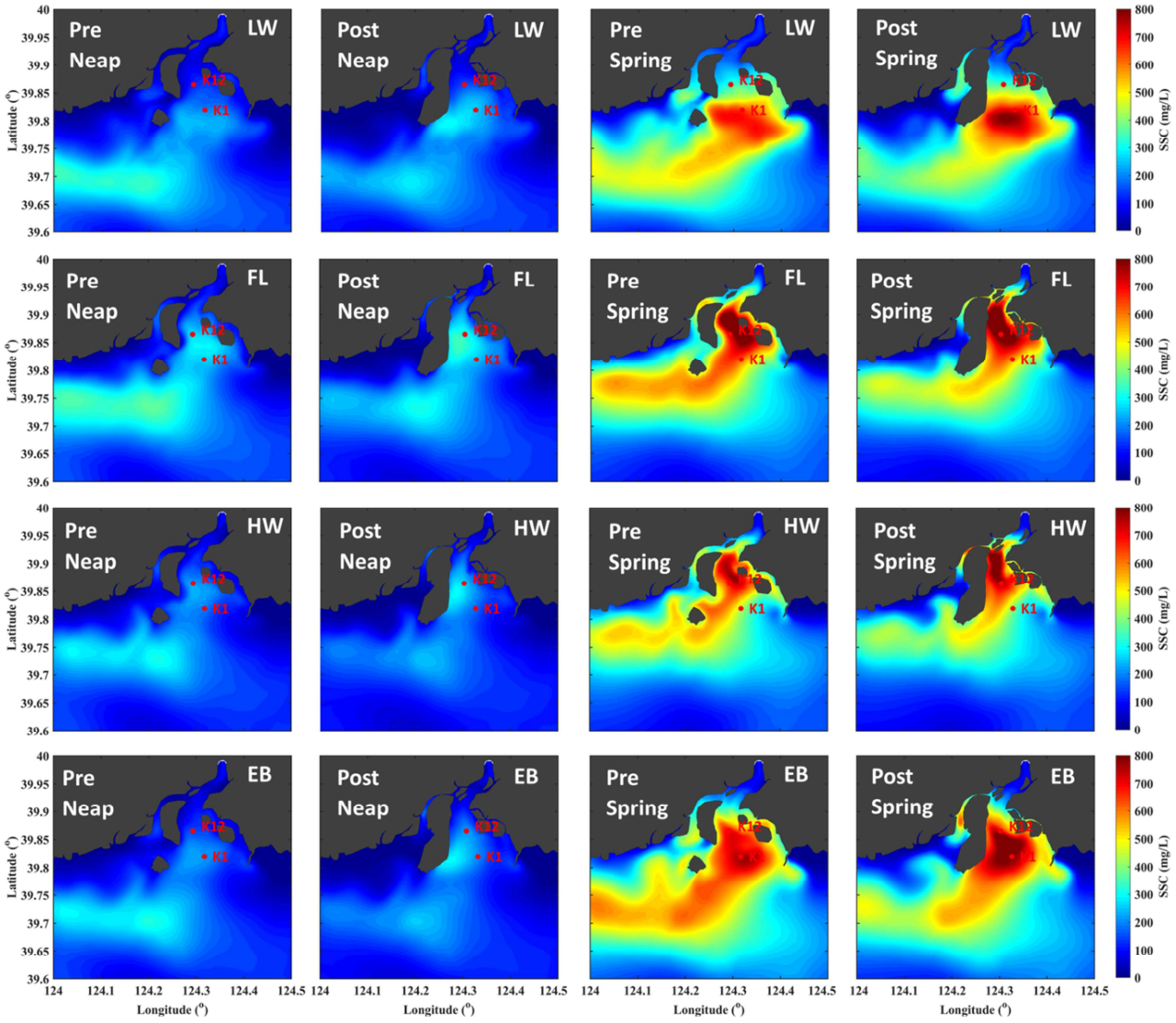
Pre Neap LW
Post Neap LW
Pre Spring LW
Post Spring LW
Pre Neap FL
Post Neap FL
Pre Spring FL
Post Spring FL
Pre Neap HW
Post Neap HW
Pre Spring HW
Post Spring HW
Pre Neap EB
Post Neap EB
Pre Spring EB
Post Spring EB
K12
K1
Latitude (°)
Longitude (°)
SSC (mg/L)

1082

1083 **Figure 12.** Model horizontal distribution of depth-averaged SSC (mg/L) for different tidal
1084 phases (LW low water; FL flood; HW high water; EB ebb) pre-reclamation (the first and third
1085 panels) and post-reclamation (the second and forth panels) during neap tide (left two panels)
1086 and spring tide (right two panels).

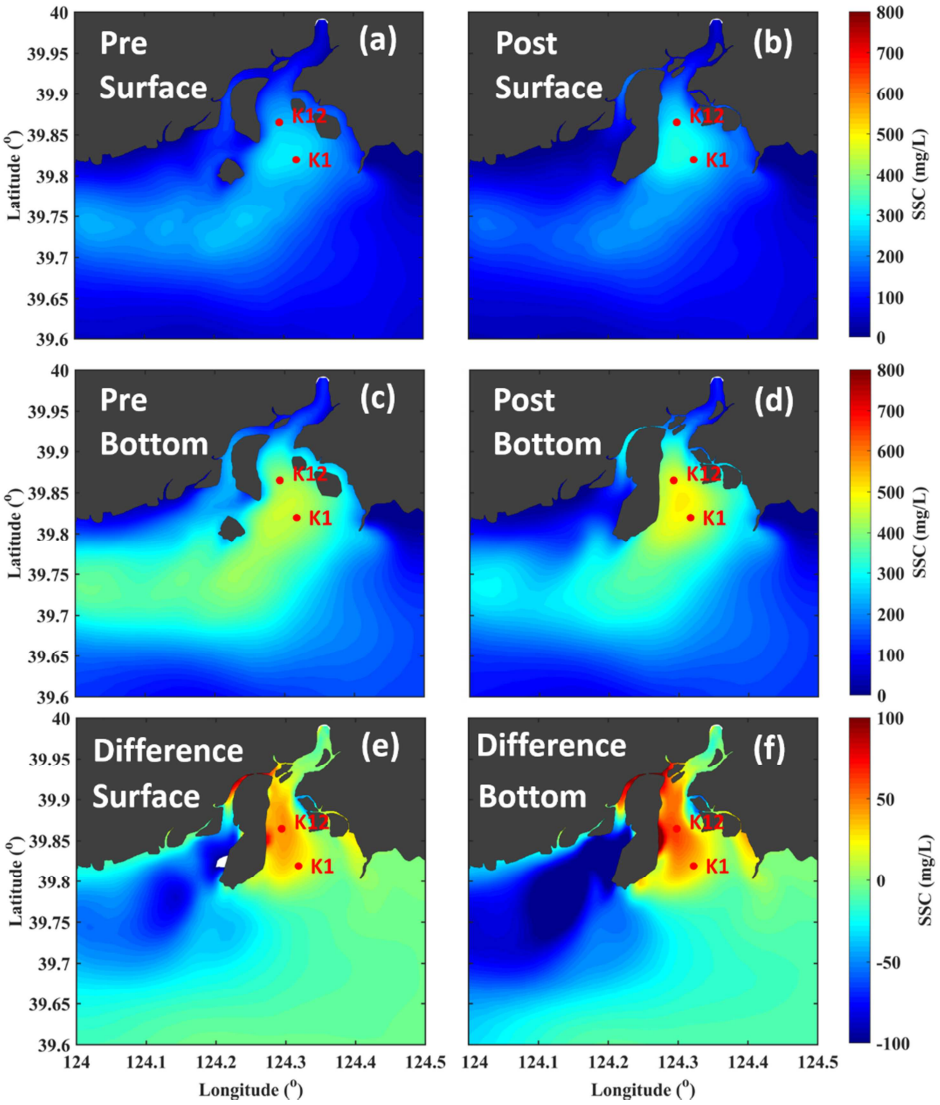

1087

Figure 13. Model horizontal distributions of monthly averaged SSC in the surface layer **(a)** pre-reclamation (Experiment 1) and **(b)** post-reclamation (Experiment 2); and in the bottom layer **(c)** pre-reclamation and **(d)** post-reclamation. Difference in the SSC distributions (Experiment 2 – Experiment 1) in the **(e)** surface layer and **(f)** bottom layer.

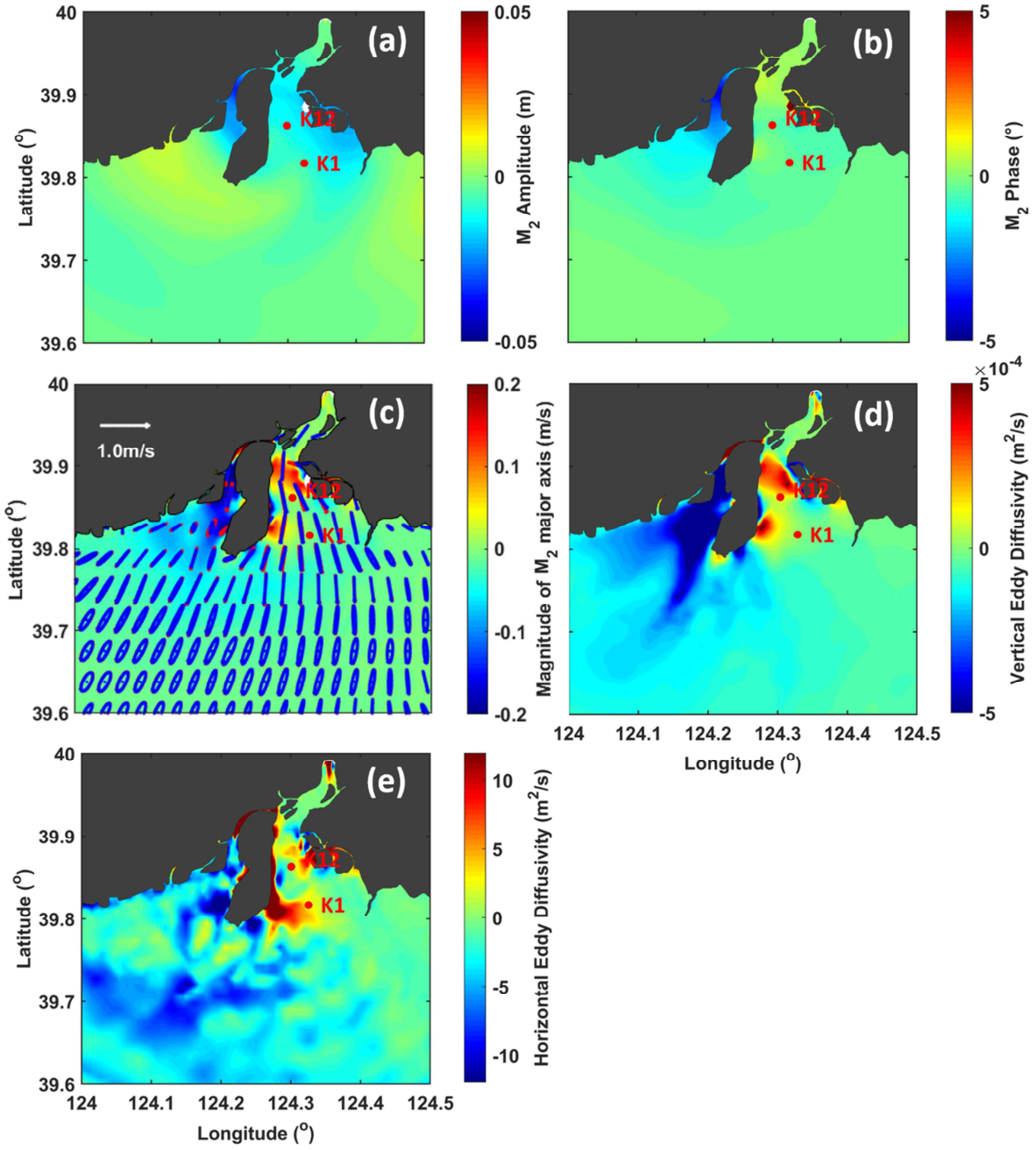

1093 **Figure 14.** Changes (Experiment 2 – Experiment 1) in the: **(a)** M2 amplitude**; (b)** M2 phase;
1094 **(c)** depth-averaged M2 major axis; **(d)** maximum monthly averaged vertical eddy viscosity;
1095 and **(e)** maximum monthly averaged horizontal eddy viscosity. The red and black ellipses in
1096 (c) are the M2 ellipses in Experiment 1 and Experiment 2, respectively.

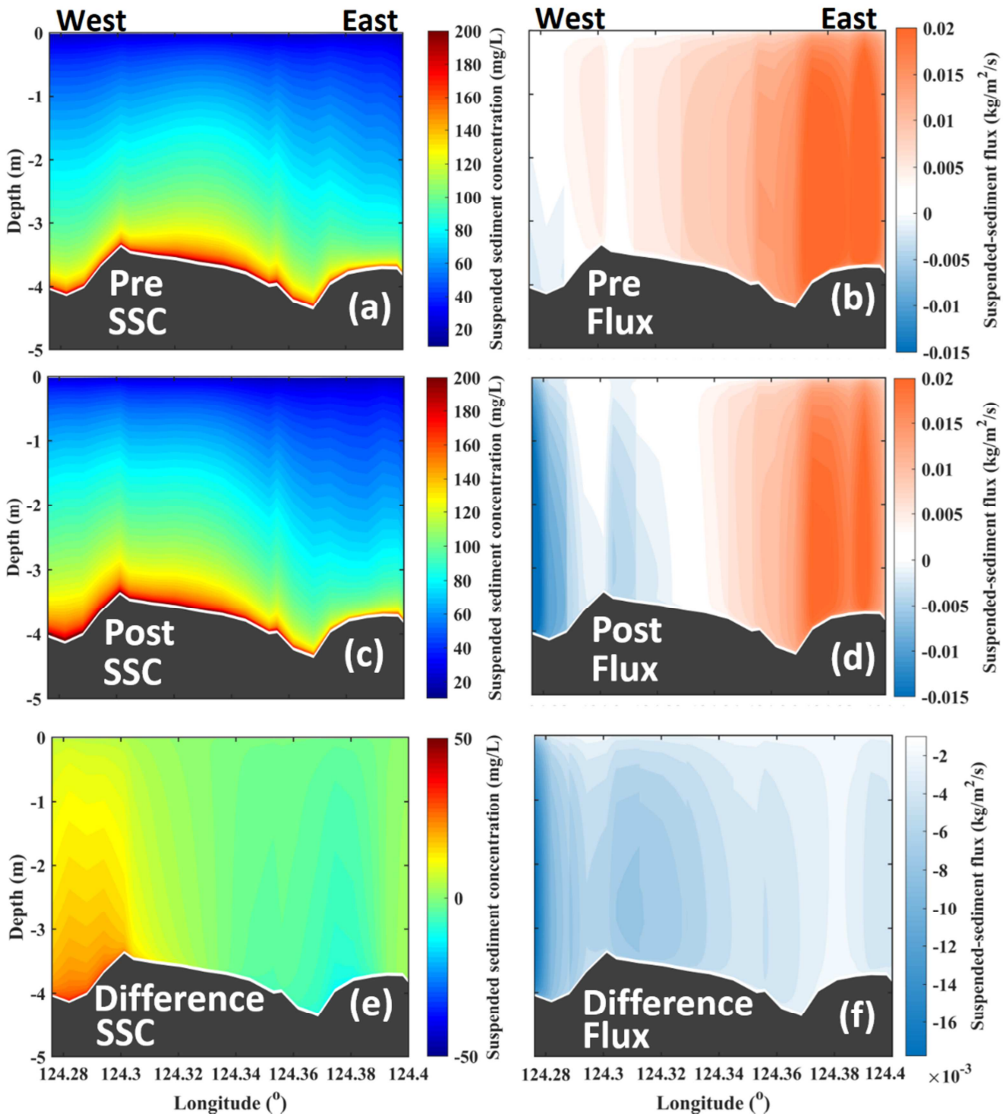

1097

Figure 15. Model monthly averaged SSC along Cross-section 1 (estuary entrance line, Fig.1) **(a)** pre-reclamation (Experiment 1) and **(c)** post-reclamation (Experiment 2); **(b)** and **(d)** the corresponding suspended-sediment fluxes. Positive and negative values represent landward and seaward directions, respectively. The left- and right-hand sides of the figures correspond respectively to the western and eastern ends of the cross-section. **(e)** shows the difference between (a) and (c): and **(f)** the difference between (b) and (d) (Experiment 2 –Experiment 1). Western side of the cross-section is near the Middle River in Fig. 1 and eastern side is close to the Western Korean Bay.

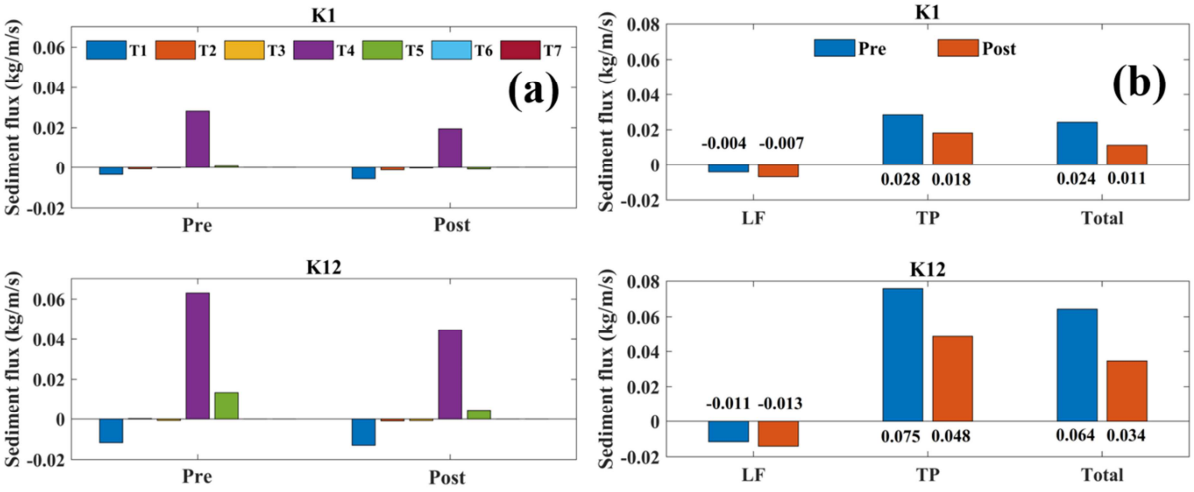

Figure 16. (a) Decomposition of the model monthly averaged sediment flux per unit width (kg/m/s) at K1 and K12 using Dyer's equation, Eq. (9) (Dyer, 1997). **(b)** As for Fig. 16a but with tidally averaged suspended sediment fluxes per unit width (kg/m/s). LF and TP denote the Lagrangian flux (T_1+T_2) and tidal pumping (T_3+T_4+T_5), respectively. Positive and negative values represent landward and seaward directions, respectively.

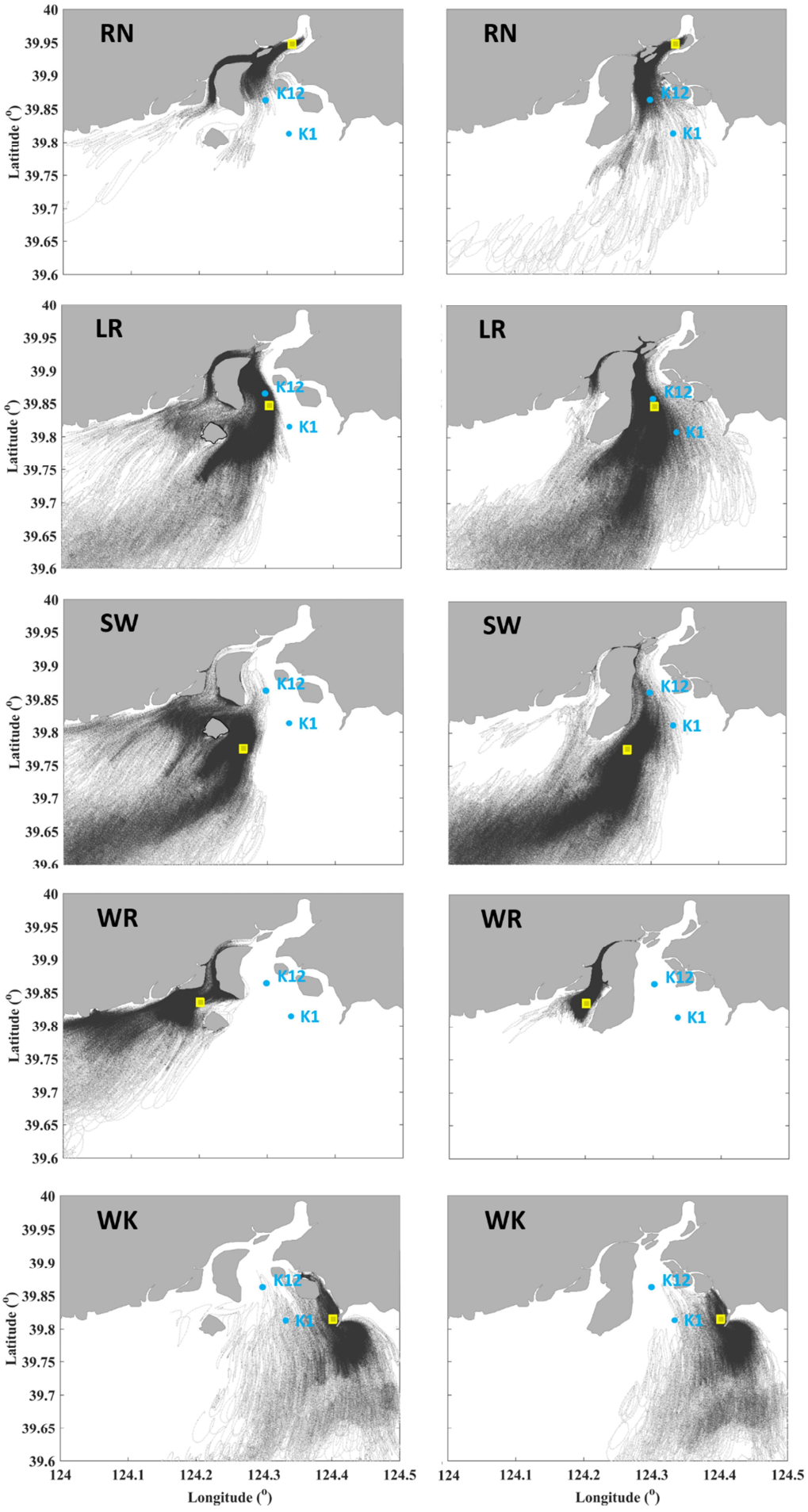
RN
LR
SW
WR
WK
K12
K1
Latitude (°)
Longitude (°)
40
39.95
39.9
39.85
39.8
39.75
39.7
39.65
39.6
124
124.1
124.2
124.3
124.4
124.5

1113 **Figure 17.** Particle-tracking results pre-reclamation (left-hand column) and post-reclamation
1114 (right-hand column). Transparent grey lines mark the trajectories of the released particles;
1115 yellow squares the source areas (release positions of the particles).

1116

1117 **Table 1.** Sectional-averaged REE concentrations (μg/g) in the YE and REE concentrations of
1118 reference samples (NASC) obtained from Taylor and McLennan (1985).

REE (μg/g) / Location	La	Ce	Pr	Nd	Sm	Eu	Gd	Tb	Dy	Ho	Er	Tm	Yb	Lu
Section A	37.81	74.04	8.27	32.40	5.43	1.00	5.29	0.67	3.51	0.74	1.98	0.29	1.83	0.27
Section B	46.72	94.19	10.28	39.79	6.66	1.12	6.31	0.80	4.45	0.92	2.49	0.36	2.30	0.34
Section C	49.43	102.05	11.44	41.84	7.23	1.28	6.08	0.72	4.26	0.86	2.39	0.34	2.16	0.34
Section D	36.48	78.70	8.21	28.48	5.01	1.13	4.55	0.64	3.14	0.53	1.52	0.24	1.46	0.22
Section E	27.95	52.67	5.94	23.08	3.89	0.86	3.65	0.44	2.41	0.51	1.37	0.22	1.27	0.18
NASC	32	73	7.9	33	5.7	1.24	5.2	0.85	5.8	1.04	3.4	0.5	3.1	0.48

1119

1120 **Table 2.** Key parameters of the model configuration.

Model parameters	**Value/method**
Model external time step	1.0 s
Bottom friction coefficient	0.0025
Horizontal diffusion	Smagorinsky scheme
Vertical eddy viscosity	M-Y 2.5 turbulent closure
Settling velocity	1.25×10^{-4} m/s
Critical bottom stress for erosion	0.1 N/m^2
Critical bottom stress for deposition	0.08 N/m^2
Erosion rate	5×10^{-6} kg/m^2/s
Number of mesh nodes and elements	3363, 6138 (Experiment 1) 2988, 5348 (Experiments 2 & 3)

1121

1122 **Table 3.** Harmonic analysis of the measured and modelled tidal constituents; measurements
1123 from the Yalu Park Hydrology Station.

Tidal Constituent	**O_1**		**K_1**		**M_2**	
	Amplitude (m)	**Phase (°)**	**Amplitude (m)**	**Phase (°)**	**Amplitude (m)**	**Phase (°)**
Measured	0.26	105.04	0.40	327.42	1.35	50.79

Model	0.22	121.03	0.40	347.08	1.49	67.88
Discrepancy	0.04	15.99	0.0	19.66	0.14	17.09

Tidal Constituent	**S_2**		**M_4**		**MS_4**	
	Amplitude (m)	**Phase (°)**	**Amplitude (m)**	**Phase (°)**	**Amplitude (m)**	**Phase (°)**
Measured	0.49	26.18	0.35	49.33	0.34	90.14
Model	0.48	32.74	0.42	47.88	0.27	83.51
Discrepancy	0.01	6.56	0.07	2.55	0.07	6.63

Table 4. Correlation coefficient (R) between model results and observation data for different variables.

	Station Y03 (spring tide)	**Station Y03 (neap tide)**	**Station Y02 (spring tide)**	**Station Y02 (neap tide)**
Water elevation	0.84	0.97	0.95	0.89
Streamwise velocity	0.90	0.88	0.83	0.85
Current direction	0.91	0.75	0.86	0.86
SSC	0.81	0.50	0.51	0.57

Highlights in “Impacts of land reclamation on sediment transport and sedimentary environment in a macro-tidal estuary.”:

- According to model results from a 3D hydrodynamic-sediment coastal model, flood dominance in a medium-scale estuary decreased after a massive land reclamation.
- Tidal-choking effect was enhanced in the main branch after reclamation, with a decreased tidal range and stronger tidal currents, which resulted in stronger mixing processes.
- The landward sediment flux caused by tidal pumping decreased significantly after the reclamation.
- A newly improved Lagrangian 3D particle-tracking model with resuspension showed sediments in the main branch were likely from different sources before reclamation but were more homogeneous with a common composition of sediment sources afterwards.
- This study proposed a multidiscipline approach to determine the sediment sources in a coastal area.

Declaration of interests

☒ The authors declare that they have no known competing financial interests or personal relationships that could have appeared to influence the work reported in this paper.

☐The authors declare the following financial interests/personal relationships which may be considered as potential competing interests: